Key Points:
- New apatite fission track and (U-Th)/He data reveal rapid exhumation in the western Danghenan Shan since ~15 Ma
- Rapid movement along the Altyn Tagh fault began at least ~15 Ma
- The north Tibet has experienced two-stage deformation in the Cenozoic

Correspondence to:
J. Yu,
jingxingyuu@gmail.com

Miocene Range Growth Along the Altyn Tagh Fault: Insights From Apatite Fission Track and (U-Th)/He Thermochronometry in the Western Danghenan Shan, China

Jingxing Yu[1,2] , **Dewen Zheng[1,3]** , **Jianzhang Pang[1]** , **Yizhou Wang[1]** , **Matthew Fox[4]** , **Pieter Vermeesch[4]** , **Chaopeng Li[1]** , **Lin Xiao[1]** , **Yuqi Hao[1]** , and **Ying Wang[1]**

[1]State Key Laboratory of Earthquake Dynamics, Institute of Geology, China Earthquake Administration, Beijing, China, [2]Department of Earth Sciences, University of Oxford, Oxford, UK, [3]State Key Laboratory of Isotope Geochemistry, Guangzhou Institute of Geochemistry, Chinese Academy of Sciences, Guangzhou, China, [4]London Geochronology Centre, Department of Earth Sciences, University College London, London, UK

Abstract The left-lateral strike-slip Altyn Tagh fault that defines the northern margin of the Tibetan Plateau plays a crucial role in accommodating the Cenozoic deformation related to the growth of plateau. However, the slip history along the fault remains highly debated. Here we report new 14–16 Ma apatite fission track (AFT) and 9–11 Ma apatite (U-Th)/He (AHe) data in the western Danghenan Shan, north Tibet. Age-elevation relationships and AFT/AHe age differences suggest a period of rapid exhumation with an average rate of 0.1–0.3 km/Ma from 16 to 9 Ma for this area. Thermal history modeling indicates that this was preceded by accelerated exhumation between the late Oligocene and middle Miocene (~15 Ma). A northward increase in AFT ages and asymmetric topography across the western Danghenan Shan indicate that the uplift and exhumation are mainly controlled by the thrust fault along the southern flank of the western Danghenan Shan. As the thrust fault is a branch of the Altyn Tagh fault, the rapid exhumation probably represents onset of the transition along the Altyn Tagh fault from left-slip motion to crustal shortening in the Dangnenan Shan region. Our findings show that the middle Miocene deformation is not only recorded in the middle and northern Qilian Shan but also in the southwestern portion of the Qilian Shan, which favors a synchronous middle-Miocene deformation model for the entire Qilian Shan.

1. Introduction

The northern Tibetan Plateau occupies about one fifth of the Tibetan-Himalayan orogeny and experiences significant crustal shortening expressed as active thrusting (Yin, 2010; Zhang et al., 2004). The temporal–spatial evolution of the northern Tibetan Plateau has important implications for the geodynamic processes of the entire plateau and its potential link to regional climate change (e.g., An et al., 2001; Clark, 2012; Molnar & Tapponnier, 1977; Tapponnier et al., 2001). Previous work has indicated that the northern Tibetan Plateau experienced deformation shortly after the India-Asia collision (e.g., Clark et al., 2010; Dupont-Nivet et al., 2004; Duvall et al., 2011; Yin & Harrison, 2000; Zhuang et al., 2011) and has undergone a phase of accelerated deformation since the Miocene (Lease, 2014; Molnar & Stock, 2009). However, the details of the spatially distributed deformation remain unclear. Competing models include progressive northward deformation, synchronously deformation, and rigid block tectonics (e.g., Burchfiel et al., 1989; Clark, 2012; Meyer et al., 1998; Molnar & Stock, 2009). Although a large body of evidence has been accumulated on the timing of deformation in north Tibet (Lease, 2014; Molnar & Stock, 2009; Zhuang et al., 2018) and along the Altyn Tagh fault (e.g., Yin et al., 2002; F. Cheng et al., 2015, 2016), the kinematics and dynamics of north Tibet remain highly debated. For example, whether the northern Tibetan Plateau has undergone gradual northward propagation in the Cenozoic (e.g., Bovet et al., 2009; Burchfiel et al., 1989; Meyer et al., 1998; Zheng et al., 2017) and whether the entire Qilian Shan has experienced a synchronous deformation in the early Cenozoic (Clark, 2012; Clark et al., 2010) or middle Miocene (Lease, 2014; Molnar & Stock, 2009). The knowledge on deformation timing in the huge area of the Qilian Shan, especially for the southwestern portion of the Qilian Shan, such as the Danghenan Shan, Daxue Shan, and the remote

region near the Hala Lake in the interior Qilian Shan, hampers the construction of a holistic deformation model for the northern Tibetan Plateau.

The Altyn Tagh fault is the longest left-lateral strike-slip fault (~1,600 km) within the India-Eurasia collision zone and defines the northern margin of the Tibetan Plateau (Molnar & Tapponnier, 1977). This makes the Altyn Tagh fault one of the most important structures in accommodating convergence between India and Eurasia. The onset of its left-lateral slip and how it was accommodated are two prominent issues for understanding the geodynamics of uplift of the Tibetan Plateau (Yin et al., 2002; Yin & Harrison, 2000; Yue & Liou, 1999). A large number of studies have investigated the geology along the Altyn Tagh fault (e.g., Chang et al., 2015; F. Cheng et al., 2015, 2016; Cowgill et al., 2003; Dupont-Nivet et al., 2004; Gilder et al., 2001; Jolivet et al., 2001; Lin et al., 2015; B. Li et al., 2017; Lu et al., 2016; Ritts et al., 2004; Shi et al., 2018; Sobel et al., 2001; Sun et al., 2005; Wang, 1997; Wu, Xiao, Wang, et al., 2012; Wu, Xiao, Yang, et al., 2012; Yin et al., 2002; Yue et al., 2001, 2004; Zhuang et al., 2011, 2018). But despite this large body of data, there is no consensus about its temporal–spatial evolution due to a lack of ideally dated geological or geomorphological records on the Cenozoic slip. Estimates for the onset of movement along the Altyn Tagh fault range from the Eocene, not long after the India-Eurasia collision (e.g., Yin et al., 2002; Jolivet et al., 2001; F. Cheng et al., 2015, 2016), to the Miocene (e.g., Chang et al., 2015; Lin et al., 2015; B. Li et al., 2017; Meyer et al., 1998; Ritts et al., 2008; Shi et al., 2018; Sun et al., 2005; Wu, Xiao, Yang, et al., 2012; Yue et al., 2001). Others have proposed a model with multiple stages of accelerated faulting to reconcile all available data along the Altyn Tagh fault (Yue et al., 2001; Yue & Liou, 1999; Zhuang et al., 2011, 2018). Nevertheless, the initiation and slip history of the Altyn Tagh fault remain the subject of much debate.

The Altyn Tagh fault truncate the westernmost Qilian Shan, which consists of several subparallel WNW-trending mountain ranges (Figure 1). Uplift of these ranges is related to the motion of the fault (Burchfiel et al., 1989; Meyer et al., 1998; Yin et al., 2002). Especially at the western end of the Qilian Shan, these elongated mountain ranges, such as the Danghenan Shan, veer counterclockwise toward the Altyn Tagh and the thrusts bounding these ranges merge with it. This suggests that the uplift of these ranges has a close relationship with the sinistral slip along the Altyn Tagh fault. Thus, the tectonic history of these ranges should provide insights into the slip history of the Altyn Tagh fault and how this slip is accommodated by crustal shortening in the Qilian Shan.

In this paper, we present thermochronological data that reveal a synchronous onset of exhumation along the Danghenan Shan in northern Tibet. Paired apatite fission track and (U-Th)/He ages from three transects and thermal modeling show that the western portion of the Danghenan Shan has experienced rapid exhumation since the middle Miocene time resulting from a thrusting along the southern range front of the western Danghenan Shan. The range-bounding thrust fault is a branch of the Altyn Tagh fault, suggesting a close link between the exhumation in the western Danghenan Shan and the sinistral slip along the Altyn Tagh fault. We infer that the onset of rapid exhumation in the western Danghenan Shan in the middle Miocene may represent the onset of transferring from the left-lateral strike slip along the Altyn Tagh fault to crustal shortening in the Qilian Shan. Our new data suggest that the middle Miocene deformation is recorded not only in the middle and northern Qilian Shan but also in the southwestern portion of the Qilian Shan.

2. Geological Setting

2.1. Danghenan Shan

The Danghenan Shan is a ~250-km long mountain range within the southwestern portion of the Qilian Shan (Figures 1 and 2, Gansu Bureau of Geology and Mineral Resources, GBGMR, 1989). It is one of several large WNW trending elongated ranges that have been interpreted as ramp anticlines bounded by crustal-scale thrusts (Burchfiel et al., 1989; Meyer et al., 1998). The regional geology of the Danghenan Shan consists of Ordovician and Silurian sandstone, conglomerate, and Paleozoic granodiorite (GBGMR, 1989). Cenozoic sediments observed along the Danghe valley and at the westernmost end of the Danghenan Shan have been assigned Oligocene-present age (Gilder et al., 2001; Sun et al., 2005; Yin et al., 2002; X. Wang et al., 2003). The Danghenan Shan is bounded by thrust faults on both of its flanks, which emplace the Paleozoic sediments or granodiorite onto the Silurian sandstone to the south, and the Cenozoic sediments to the north (Figure 2, GBGMR, 1989). Active thrusts cut Quaternary alluvial surfaces north and south of the Danghenan Shan, showing remarkable fault scarps on satellite imagery and in the field (Meyer et al., 1998; Shao et al.,
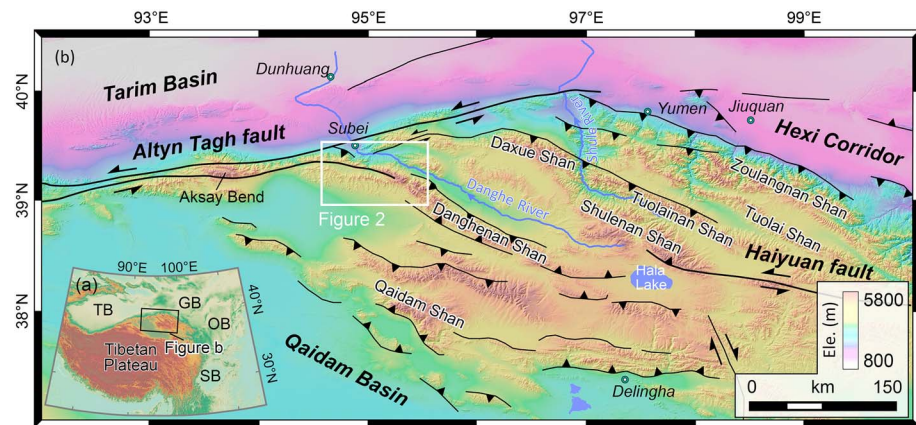
Figure 1. (a) Map of the Tibetan Plateau and surrounding regions, showing the location of (b). Abbreviations: TB—Tarim Basin; GB—Gobi-Alashan Block; OB—Ordos Block; SB—Sichuan Basin. (b) Topographic map of the northern Tibetan Plateau with major structures, the white rectangle shows the location of the study area; locations of active faults are from Tapponnier et al. (2001).

2017). At the western end of the Danghenan Shan, the Altyn Tagh fault is separated into two branches, forming the northern and southern Altyn Tagh faults (Figure 1). The continuous NE-trending northern Altyn Tagh fault marks the topographic difference between the Tarim Basin and Qilian Shan, whereas the southern Altyn Tagh fault bends clockwise from NE to EW and marks the southern range front of the Danghenan Shan (Figure 2).

2.2. Subei Basin

To the northwest of the Danghenan Shan, the Subei Basin, which is cut by the northern Altyn Tagh fault, lies within the range front (Figure 2). The Danghe River, flowing westward out of the Tibetan Plateau, transfers materials from the Tuolainan Shan and Danghenan Shan to the Subei Basin and further northwest to the Tarim Basin. Thus, the depositional history of the Subei Basin provides insights into the tectonic evolution of the Danghenan Shan. Cenozoic deposits in the Subei Basin are well exposed in the Tiejianggou and Xishuigou sections (Figure 2) and were divided into three upward coarsening units based on mammalian fossils and lithology: (1) Oligocene Paoniuquan Formation, basal, reddish mudstone, clayey, sandy silts, and sandstone; (2) early-middle Miocene Tiejianggou Formation, purplish red mudstone, sandy silt, and
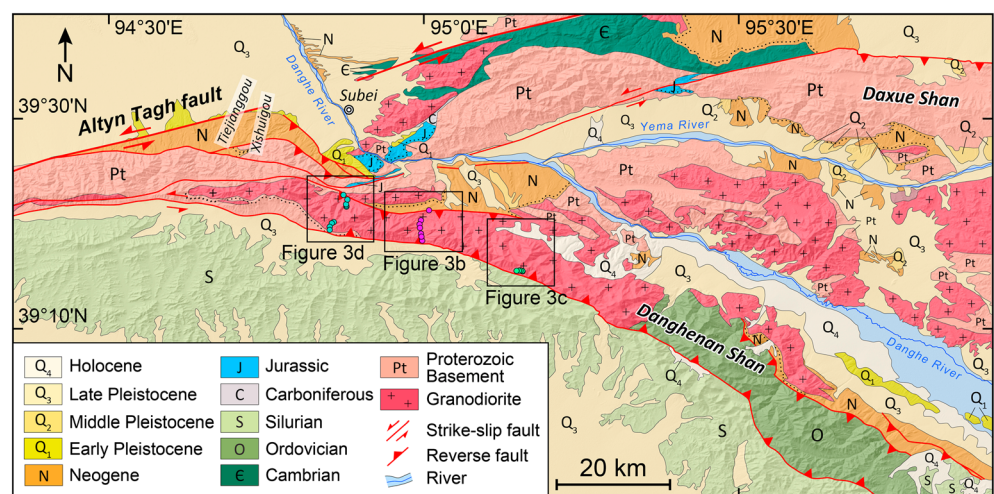
Figure 2. Geological map of the western Danghenan Shan and adjacent areas. The geological map is modified from GBGMR (1989). Red lines are major faults in the region. Black boxes show the locations of the three sampling transects —magenta dots for Transect 1, green dots for Transect 2, and cyan dots for Transect 3.

sandstone that gradually coarsens to conglomerate; and (3) an unnamed late Miocene to Pliocene formation, coarse conglomerate interbedded with sandstone (Bohlin, 1937; Gilder et al., 2001; Sun et al., 2005; Yin et al., 2002; X. Wang et al., 2003). The initiation of Cenozoic deposition and emergence of coarse conglomerate in the basin were interpreted as marking the onset of accelerated deformation along the Altyn Tagh fault, and the initiated uplift of the Danghenan Shan. Based on the magnetostratigraphic results on the initial Cenozoic deposition in the Xishuigou section, Yin et al. (2002) considered the appearance of the early Oligocene (~33 Ma) fine-grained red mudstone as evidence of initial crustal shortening, suggestive of an early deformation in the Danghenan Shan. In contrast, X. Wang et al. (2003) presented new paleontological data in the Xishuigou section and the Tiejianggou section, which is only ~5 km to the Xishuigou section and has similar depositional sequence, and reinterpreted the published magnetostratigraphy to propose an early Miocene age for these red beds. Adding further samples in the Tiejianggou section, Sun et al. (2005) constrained the deposits to be much younger (<22.8 Ma). These authors suggest that the accumulation of coarse conglomerate began ~13.7 Ma, marking the initial tectonic uplift in this region. They argue for a low relief lacustrine environment for the Subei Basin before 13.7 Ma, which means no significant uplift occurred in the Subei and Danghenan Shan region during this period. This is supported by an inferred provenance change at ~14 Ma based on detrital apatite fission track data from the same section, which is interpreted as the result of the uplift of the western Danghenan Shan (Lin et al., 2015). Direct dating on the initial timing of accelerated uplift of the Danghenan Shan come from an age-elevation profile in the northern range front of the western Danghenan Shan, which shows consistent (U-Th)/He ages between 7.0 and 8.3 Ma, suggesting that the Danghenan Shan experienced rapid uplift at or slightly before that time (Zhuang et al., 2018).

3. Methods

The apatite fission track (AFT) and apatite (U-Th)/He (AHe) methods have annealing/closure temperatures ranging from 60 to 110/120 °C (Gleadow et al., 2002; Ketcham et al., 2007) and partial retention zone of ~40–80 °C (Farley, 2000; Wolf et al., 1996, 1998), respectively, thus providing constraints on exhumation histories of the shallow crust at ~2- to 5-km depth. Kinetic models for thermal annealing of apatite fission tracks and Helium volume diffusion have been well developed (Flowers et al., 2009; Green et al., 1986). We utilized the elevation dependency of AFT and AHe ages and thermal-kinematic modeling to determine the onset and duration of accelerated thrust-related exhumation in the western Danghenan Shan.

To investigate exhumation history along the western Danghenan Shan, we collected 21 samples from three transects (Transects 1 to 3) within the hanging wall (Figures 2 and 3). All samples were collected from Paleozoic granodiorites (GBGMR, 1989). We obtained 19 AFT ages and 18 mean AHe ages for these three transects (Tables 1 and S1 and S2 in the supporting information). AFT data for all samples passed the χ^2 test and show tightly clustered ages (age dispersions close to 0) of single grains. AHe ages are average of >3 aliquots. QTQt (v 5.4.0; Gallagher, 2012) was used to infer the most probable exhumation history from our data.

3.1. Sampling Locations

Transect 1 was collected along a northward flowing tributary of the Danghe River that approximately perpendicular to the range axis (Figure 3b). Seven samples were collected within the hanging wall of the thrust fault (F1) that lies along the base of the southern flank of the Danghenan Shan. The fault defines a sharp boundary between the Paleozoic granodiorites and Quaternary fluvial/alluvial sediments, forming a sharp topographic difference of ~1,000 m and faceted range front. In contrast, the topography is much gentler along the northern flank of the mountain range. Although a reverse fault (F2) was mapped along the boundary between the granodiorites and Neogene sediments (Figure 2), there is no geomorphic evidence suggesting that the fault is still active.

Transect 2 is ~15 km to the east of Transect 1 (Figure 3a). Five samples were collected along an elevation profile ranging from 4,342 to 4,829 m within 1 km in horizontal distance to the southern range-front fault (F1). The fault juxtaposes the Paleozoic granodiorites over the Silurian sandstone. Similarly, the topography is asymmetric and the northern flank of the mountain range is much gentler than the south.

Transect 3 is located at the western end of the Danghenan Shan, adjacent to the Altyn Tagh fault and Subei Basin (Figure 2). This transect comprises nine samples along a N-S profile across the western Danghenan
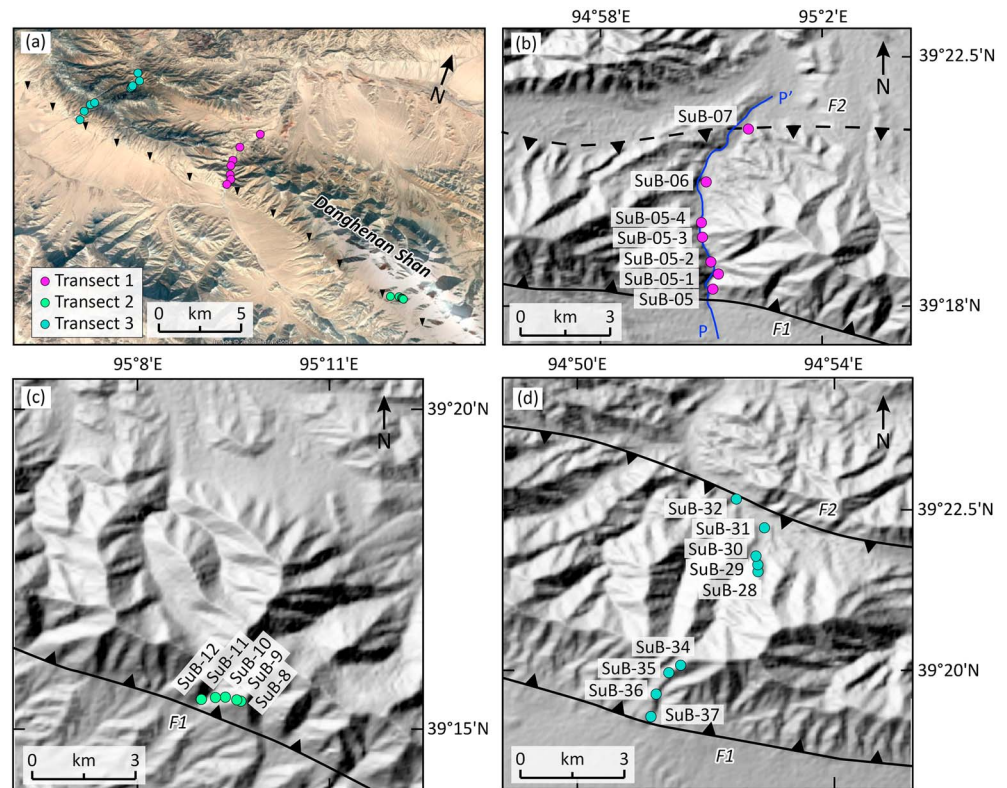
Figure 3. (a) Satellite image of the western Danghenan Shan, showing sample locations for the three transects. Transect 1 contains seven samples (magenta dots) collected along a tributary of the Danghe River perpendicular to the range front; Transect 2 (green dots) is a vertical transect within 1.5 km from the range-bounding thrust fault of the western Danghenan Shan; Transect 3 has nine samples (cyan dots) distributed across the western end of the Danghenan Shan, of which five are situated on the northern flank and the remaining four from the southern flank. Reverse triangles show the trace of the active thrust fault along the southern range front of the Danghenan Shan. No linear structure was observed along the southern range front. The topography of the western Danghenan Shan is asymmetric with the mountain ridge shifted toward the southern front. (b) Shaded relief map of Transect 1. A continuous linear active fault trace (F1) can be observed along the southern range front, whereas the geological boundary (F2) between the granodiorite and Neogene sediments (Figure 2) along the northern range front cannot be traced in the field or the satellite imagery. (c) Shaded relief map of Transect 2. (d) Shaded relief map of Transect 3, which consists of two elevation profiles.

Shan (Figure 3d). Four of these were collected from the southern flank of the mountain range and five from the northern flank. All samples are from the Paleozoic granodiorites. The granodiorites intruded at this locality are bounded by thrust faults along both the southern and northern range front. The northeastward extension of the southern Altyn Tagh fault (F1) goes along the base of southern flank of the mountain range and fresh surface ruptures were observed in the field. Meanwhile, another north-verging thrust fault (F2; Yin et al., 2002), extends along a valley in the northern flank of the mountain. The mountain ridge is biased toward the south, closer to F1 rather than F2.

3.2. AFT Sample Preparation and Analytical Techniques

Two AFT ages (SuB-05-2 and SuB-05-4) were measured using laser ablation inductively coupled plasma mass spectrometry fission track (LA-ICP-MS-FT) method (Pang et al., 2017) and the remaining samples using the external detector method (Gleadow, 1981). All the fission track ages were analyzed at the Institute of Geology, China Earthquake Administration. Track length distributions were measured at the School of Earth Sciences, University of Melbourne. Apatite crystals were hand-picked and then mounted on epoxy slides with araldite epoxy. Spontaneous fission tracks were etched in 5.5 M HNO_3 at 21 °C for 20 s (Donelick et al., 1999). Induced fission tracks were recorded in low-U mica, using CN5 as a dosimeter. After irradiation at the 492 reactor, China Institute of Atomic Energy, the mica and standard glass were etched with 40% HF at 20 °C for 40 min. A Zeta (ζ) value of 353 ± 10 was determined using Durango

Table 1
Sample Locations and Apatite Fission Track and (U-Th)/He Ages

Sample ID	Longitude (°E)	Latitude (°N)	Elevation (m)	AFT age Central age ± 1σ (Ma)	AFT length ML ± 1σ (μm)	SD$_{ML}$ (μm)	AHe age Corrected age ± 1σ (Ma)
Transect 1							
SuB-05	95.001	39.305	3,209	14.97 ± 0.89	13.9 ± 0.2	1.4	8.7 ± 0.3
SuB-05-1	95.002	39.310	3,193	NA	NA	NA	10.88 ± 1.17
SuB-05-2	95.000	39.313	3,156	24.1 ± 1.3	NA	NA	9.49 ± 1.86
SuB-05-3	94.997	39.321	3,134	NA	NA	NA	10.79 ± 0.79
SuB-05-4	94.997	39.325	3,080	18.8 ± 1.0	NA	NA	9.7 ± 1.11
SuB-06	94.999	39.337	3,030	45.9 ± 1.3	11.3 ± 0.2	1.9	11.8 ± 1.9
SuB-07	95.011	39.353	2,920	58.5 ± 1.6	11.7 ± 0.1	1.2	20.8 ± 3.8
Transect 2							
SuB-08	95.160	39.257	4,829	15.6 ± 0.8	13.8 ± 0.2	1.7	NA
SuB-09	95.159	39.258	4,710	15.5 ± 0.7	13.6 ± 0.2	1.9	10.5 ± 0.3
SuB-10	95.156	39.258	4,601	14.3 ± 0.7	14.1 ± 0.1	1.4	10.4 ± 1.2
SuB-11	95.154	39.258	4,493	14.5 ± 0.8	14.0 ± 0.1	1.3	9.1 ± 1.2
SuB-12	95.150	39.258	4,342	12.3 ± 0.8	14.2 ± 0.1	1.3	9.2 ± 0.8
Transect 3							
SuB-28	94.88	39.359	3,675	14.6 ± 0.6	14.4 ± 0.1	1.1	10.7 ± 0.5
SuB-29	94.88	39.361	3,494	14.2 ± 0.7	14.1 ± 0.1	1.2	10.5 ± 0.5
SuB-30	94.88	39.363	3,371	14.3 ± 0.9	14.3 ± 0.1	1.1	9.7 ± 0.7
SuB-31	94.882	39.370	3,187	18.8 ± 1.9	14.0 ± 0.2	1.3	NA
SuB-32	94.876	39.378	3,060	14.4 ± 1.0	13.4 ± 0.2	1.6	NA
SuB-34	94.86	39.335	4,358	14.1 ± 0.8	14.4 ± 0.1	1.1	10.3 ± 0.4
SuB-35	94.857	39.333	4,201	14.2 ± 0.8	14.4 ± 0.1	1.1	10.8 ± 0.8
SuB-36	94.854	39.327	4,054	13.8 ± 0.8	14.3 ± 0.1	1.3	9.7 ± 0.5
SuB-37	94.854	39.320	3,829	14.3 ± 0.9	14.0 ± 0.1	1.4	11.4 ± 1.0

Note. ML = nonprojected mean confined track length; SD$_{ML}$ = standard deviation for ML. NA = not applicable.

apatite and Fish Canyon Tuff as age standard (Hurford & Green, 1983). To compensate the low track density of our samples, a Cf-252 source was used to increase the number of confined tracks (Donelick & Miller, 1991). D_{par} (diameter of etch figures parallel to the crystallographic *c* axis) measurements were taken to constrain the annealing kinetics of apatite (Donelick et al., 1999). Full results are reported in Tables 1 and S1 in the supporting information.

3.3. Apatite (U-Th)/He (AHe) Sample Preparation and Analytical Techniques

Apatite (U-Th)/He analyses were conducted at the Institute of Geology, China Earthquake Administration using standard procedures (Farley & Stockli, 2002), which can be divided into three steps: measurement of grain dimensions, measurement of He content, and measurement of U and Th content. (1) Measurement of grain dimensions: euhedral apatite crystals with minimum dimension ≥80 μm free of inclusions were hand-picked from sample separates, then grain dimensions were measured under 100X binocular microscope; (2) measurement of He content: The picked apatite grains and Durango apatite age standards were individually wrapped in Pt tubes. Then, extraction of He and isotope analysis were completed on an Alphachron instrument. Samples were placed in a Cu planchet and degassed in vacuo by Nd-YAG laser heating (8A current) for 5 min. This process was done at least twice to confirm complete ^{4}He extraction. The ^{4}He was spiked with ^{3}He and analyzed by a quadrupole mass spectrometer; (3) measurement of U and Th contents: After He analysis, the degassed apatite grains were retrieved and transferred into vials containing a mixed spike of ^{235}U, ^{230}Th (25 μl) in 7 mol/L HNO$_3$ for dissolution. The concentration of ^{235}U, ^{230}Th spike are 15, 5 ng/ml, respectively. The ^{235}U/^{238}U and ^{230}Th/^{232}Th isotopic ratios in the spike are 838 ± 7, 10.45 ± 0.05, respectively. Vials were heated to 120 °C for 1 hr on hot plate and standing for 4 hr at room temperature to insure complete dissolution. Then, Milli-Q water was added into vials to dilute the solution to 2.5 ml. Finally, spiked standard solution, spiked sample solution, and blank, which containing 7 mol/L HNO$_3$ (25 μl) and empty Pt tube, were measured on Agilent 7900 ICP-MS (inductively coupled plasma-mass spectrometer). He apparent ages were calculated iteratively according to the equation:
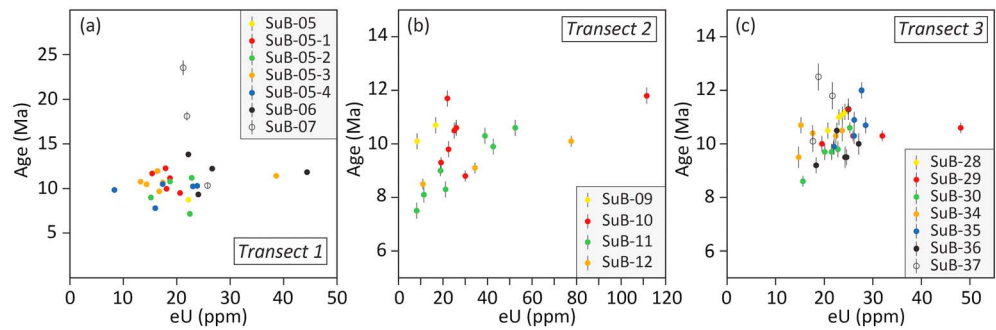
Figure 4. Corrected AHe ages versus effective uranium content [eU]. Except for samples SuB-11 and SuB-30, none of the single-grain AHe distribution display a clear relationship with eU content, indicating no significant effect of radiation damage among grains.

^{4}He = 8(^{238}U) [exp ($\lambda_{238}t$) − 1] + 7(^{235}U) [exp ($\lambda_{235}t$) − 1] + 6(^{232}Th) [exp ($\lambda_{232}t$) − 1] and corrected for α ejection (Ketcham et al., 2011). AHe ages were determined from two to seven aliquots per sample, yielding reproducible AHe data for most of the samples. No age-eU correlation was observed (Figure 4), suggesting of insignificant radiation damage (Flowers et al., 2009).

Overall we obtained 82 AHe ages for our 21 samples (Tables 1 and S2 in the supporting information). Replicating analyses of 18 grains of Durango apatite yielded a consistent ratio of Th/U (with mean value of 21.4 ± 1.1) and mean apparent age of 31.92 ± 1.59 Ma (Y. Wang, Zheng, Wu, et al., 2017), which is in good agreement with the reference of 31.02 ± 0.22 (McDowell et al., 2005).

3.4. Thermal Modeling

We use QTQt (v 5.4.0; Gallagher, 2012) to further investigate the thermal evolution of samples in the western Danghenan Shan. QTQt extracts time–temperature paths from complex thermochronological data sets based on the Bayesian transdimensional Markov chain Monte Carlo inversion scheme (Gallagher, 2012; Vermeesch & Tian, 2014). AFT ages and projected fission track lengths with D_{par} as kinetic parameter are included in the fission track annealing model of Ketcham et al. (2007). Flower et al.'s (2009) Radiation Damage Accumulation and Annealing Model was used for helium diffusion modeling. The present temperature was set to 10 ± 10 °C. The present geothermal gradient is in a broad range of 30 ± 30 °C/km, which is based on the current geothermal gradient of 20–25 °C/km in north Tibet (Hu et al., 2000) and possible effect on shallow isotherms by exhumation (Ehlers et al., 2005). The paleotemperature offset is set as 15 ± 15 °C and can vary over time. As there is no further information on cooling history, we do not impose any other temperature constraint. All models run with 200,000 iterations for burn-in process and 200,000 for posterior ensemble. There is no obvious trend in the likelihood/posterior chain for all models.

4. Results

4.1. AFT and AHe Ages

4.1.1. Transect 1

The southernmost sample (SuB-05) has a relatively young (14.97 ± 0.89 Ma) AFT age and a mean track length of 13.9 ± 0.2 μm (Figure 5b and Table 1). At ~900 m to the north of SuB-05, sample SuB-05-2 has an older AFT age of 24.1 ± 1.3 Ma. Sample SuB-05-4, which lies ~1.3 km to the north of SuB-05-2, has an AFT age of 18.8 ± 1.0 Ma, whereas the AFT ages for the northernmost two samples (SuB-06, 07) are much older (45.9 ± 1.3 Ma and 58.5 ± 1.6 Ma) and mean track lengths are shorter (11.3 ± 0.2 and 11.7 ± 0.1 μm). In contrast, six AHe ages derived from the southern six samples fall between 9 and 12 Ma, while the northernmost sample (SuB-07) has an AHe age of 20.8 ± 3.8 Ma. In conclusion, the AFT ages increase northward, in tandem with the northward shortening fission track lengths. In contrast, the AHe ages agree within error across the entire sampling transect except for sample SuB-07.
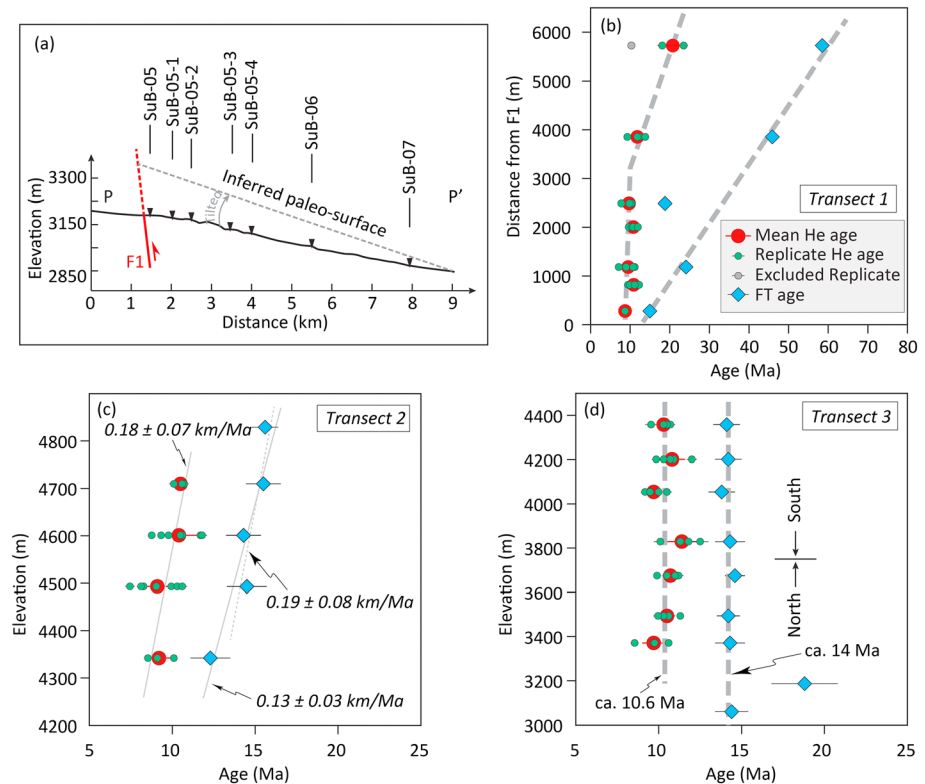
Figure 5. (a) A schematic structural model along profile PP′ in Transect 1, showing the exhumation of the hanging wall of the thrust fault (F1). The tilted block is structurally controlled by the north-dipping F1. (b) apatite fission track (AFT) and AHe ages in Transect 1 plotted against distance from the thrust fault (F1) along the southern range front of the western Danghenan Shan. The AFT ages in Transect 1 increase monotonically northward, while the AHe ages are constant within error across the entire sampling transect except for sample SuB-07 with AHe age of 20.8 ± 3.8 Ma. Assuming a single titled block model as showed in (a), the regressed dash lines in distance-age plot represent relative exhumation rates. (c) Both AFT and AHe age-elevation relationships in Transect 2 indicate consistent exhumation rates: 0.18 ± 0.07 km/Ma for AHe data, 0.19 ± 0.08 km/Ma for the upper four AFT ages and 0.13 ± 0.03 km/Ma for all the AFT data; (d) AFT ages in Transect 3 from both the northern and southern flanks of the western Danghenan Shan are clustered at ~14 Ma, except for sample SuB-31, which has an AFT age of 18.8 ± 1.9 Ma. The AHe ages are ~10.6 Ma within error.

4.1.2. Transect 2

AFT ages increase monotonically with elevation, ranging between 12.3 ± 0.8 and 15.6 ± 0.8 Ma (Figure 5c; Table 1). Mean track lengths vary between 13.6 ± 0.2 and 14.2 ± 0.1 μm with narrow standard deviations (1.3–1.9 μm), suggestive of rapid cooling through the partial annealing zone. All five samples were collected within narrow horizontal distance of <1 km adjacent to the thrust fault along the southern flank of the western Danghenan Shan. We estimate an exhumation rate of 0.1–0.3 km/Ma from the slope of a best fitting line in the age-elevation plot by least squares fitting. AHe ages derived from the lower four samples in this transect range from 9.1 ± 0.8 to 10.5 ± 0.3 Ma (Table 1). The slope of the latter age-elevation relationship suggests an exhumation rate of 0.18 ± 0.07 km/Ma, which agrees well with that derived from the AFT data.

4.1.3. Transect 3

Eight out of nine samples in this transect yield ~14 Ma AFT ages (Figure 5d and Table 1). Only sample SuB-31 yields an older age of 18.8 ± 1.9 Ma. AHe ages for seven samples are ca. 10.6 Ma. Neither the AFT nor the AHe ages vary significantly beyond the analytical uncertainties. Mean track lengths vary between 13.4 ± 0.2 and 14.4 ± 0.1 μm.

4.2. Thermal Modeling

Due to the samples in Transect 1 were collected along a tributary of the Danghe River and not along an elevation profile, which would produce unequal uplift rates, AFT and AHe data for each sample in this transect were modeled separately. The inverse modeling for SuB-05 and SuB-05-4 indicates steady cooling since
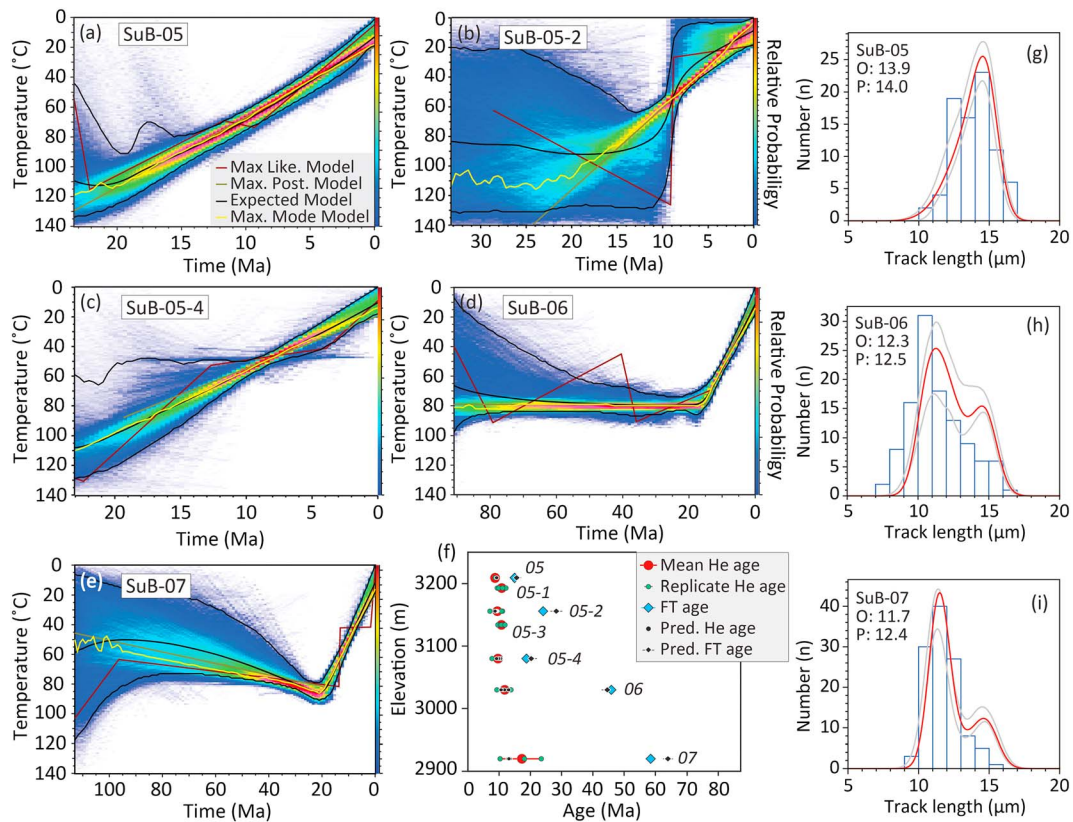
Figure 6. QTQt inverse models for Transect 1. (a–e) Thin black lines show the 95% credible intervals for the expected model. (f) Observed and predicted age-elevation distributions, inferred from the expected model. (g–i) Comparison between observed (o) and predicted (p) projected fission-track length. Histograms show the observed projected fission-track length distribution and the red curves denote the predicted distribution, with 95% credible intervals marked by the gray curves.

~20 Ma (Figure 6). These two samples passed through the partial annealing zone (PAZ) rapidly and have been totally annealed, and do therefore not constrain the onset of rapid cooling. The cooling history for SuB-05-2 is poorly constrained. The Expected Model suggest a rapid cooling since ~10 Ma, whereas the Maximum Mode Model reveals a similar rapid cooling history as SuB-05 and SuB-05-4. SuB-06 and SuB-07 have younger AHe ages but much older AFT ages, suggesting that they experienced a relatively slow cooling history between the early Cenozoic and middle Miocene. They are most likely to reveal the onset timing of rapid cooling. The Expected Models of SuB-06 and SuB-07 are similar. They stay in the PAZ and suggest slight reheating from the late Cretaceous to ~20–15 Ma, followed by rapid cooling with a constant cooling rate until the present.

Transect 2 consists of five samples whose age-elevation profile indicates rapid exhumation of 0.1–0.3 km/Ma from ~16 to 9 Ma. This is consistent with a long-term average exhumation rate of 0.2–0.3 km/Ma since ~16 Ma, suggesting that these samples may have passed through the PAZ rapidly and were then exhumed toward the surface with a nearly constant rate. The AFT and AHe ages from each sample are modeled jointly. The inverse modeling reveals reheating from the late Oligocene to ~16–17 Ma and monotonic cooling after that (Figure 7). The predicted ages and projected fission track lengths from the Expected Model match the data very well for all the samples in the elevation transect. The inverse models and long fission track lengths suggest that these samples went through the PAZ rapidly and that the onset of rapid cooling occurred during the early Miocene (~16–17 Ma).

As discussed previously, Transect 3 may have undergone interior deformation. Therefore, the samples are modeled separately. The results of this exercise are similar to those for Transect 1, indicating a phase of monotonic cooling since 15–20 Ma, followed by a slight decrease in cooling rate for some samples since ~10 Ma (Figure 8).
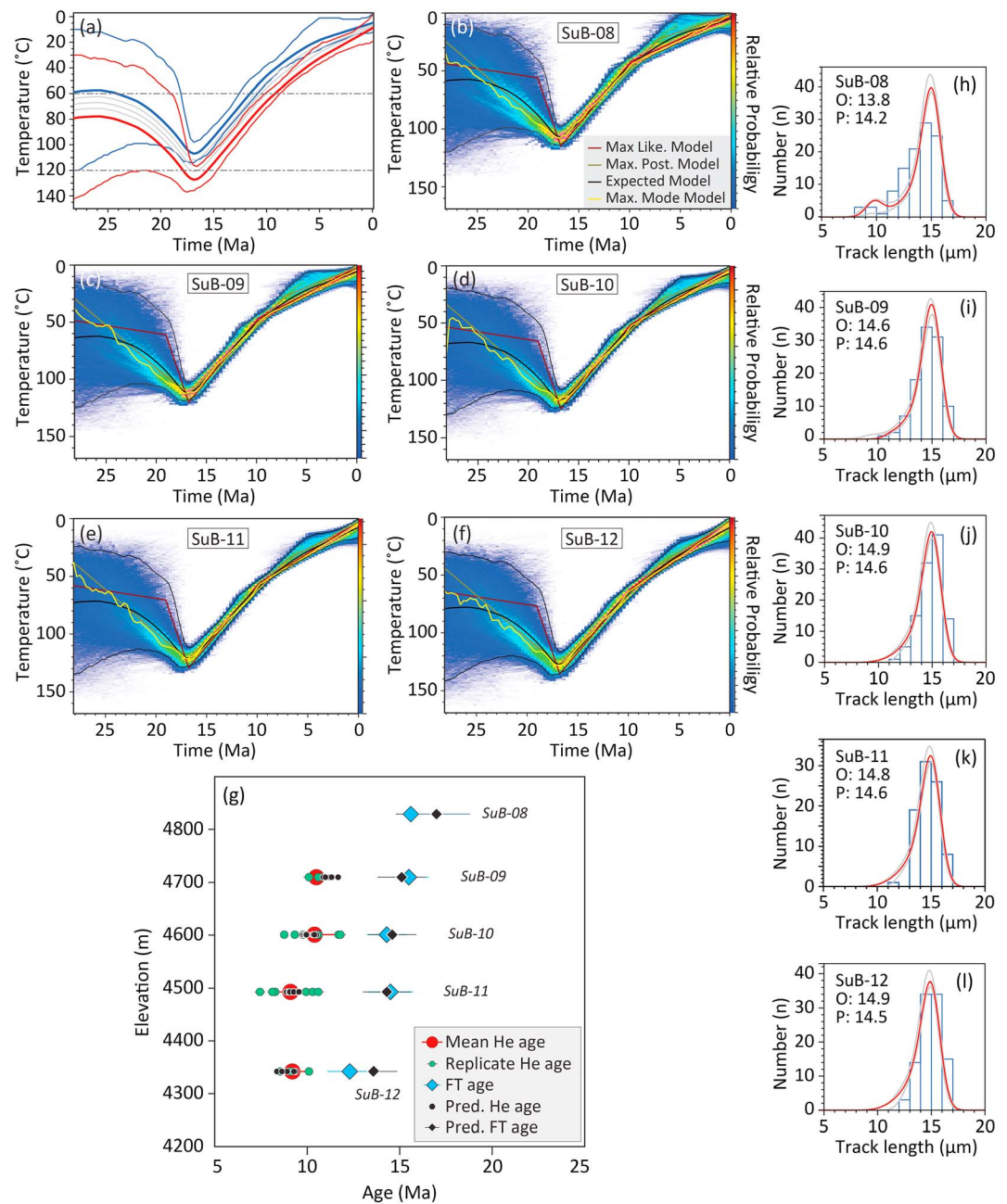
Figure 7. (a) Time–temperature history of Transect 2 obtained by QTQt modeling. Blue and red lines correspond to the upper- and lowermost samples; thin blue and red lines represent their respective 95% credible intervals. Gray lines represent the cooling histories of the three intermediate samples. (b–f) QTQt thermal history inversions for Transect 2. Thin black lines show the 95% credible intervals of the expected model. (g) Comparison between observed and predicted age-elevation distribution. All the predicted AHe and apatite fission track (AFT) ages are from the expected model. (h–l) Comparison between observed (o) and predicted (p) projected fission-track length.

5. Discussion

5.1. Timing of Rapid Exhumation in the Western Danghenan Shan

The 4–5 Ma difference between all paired AFT and AHe ages from individual samples in Transect 2 suggests a cooling rate of 9 ± 4 °C/Ma from 15.6 ± 0.8 to 9.1 ± 1.2 Ma, which is supported by thermochronological modeling. Assuming an appropriate geothermal gradient of 20–25 °C/km in north Tibet (Hu et al., 2000),
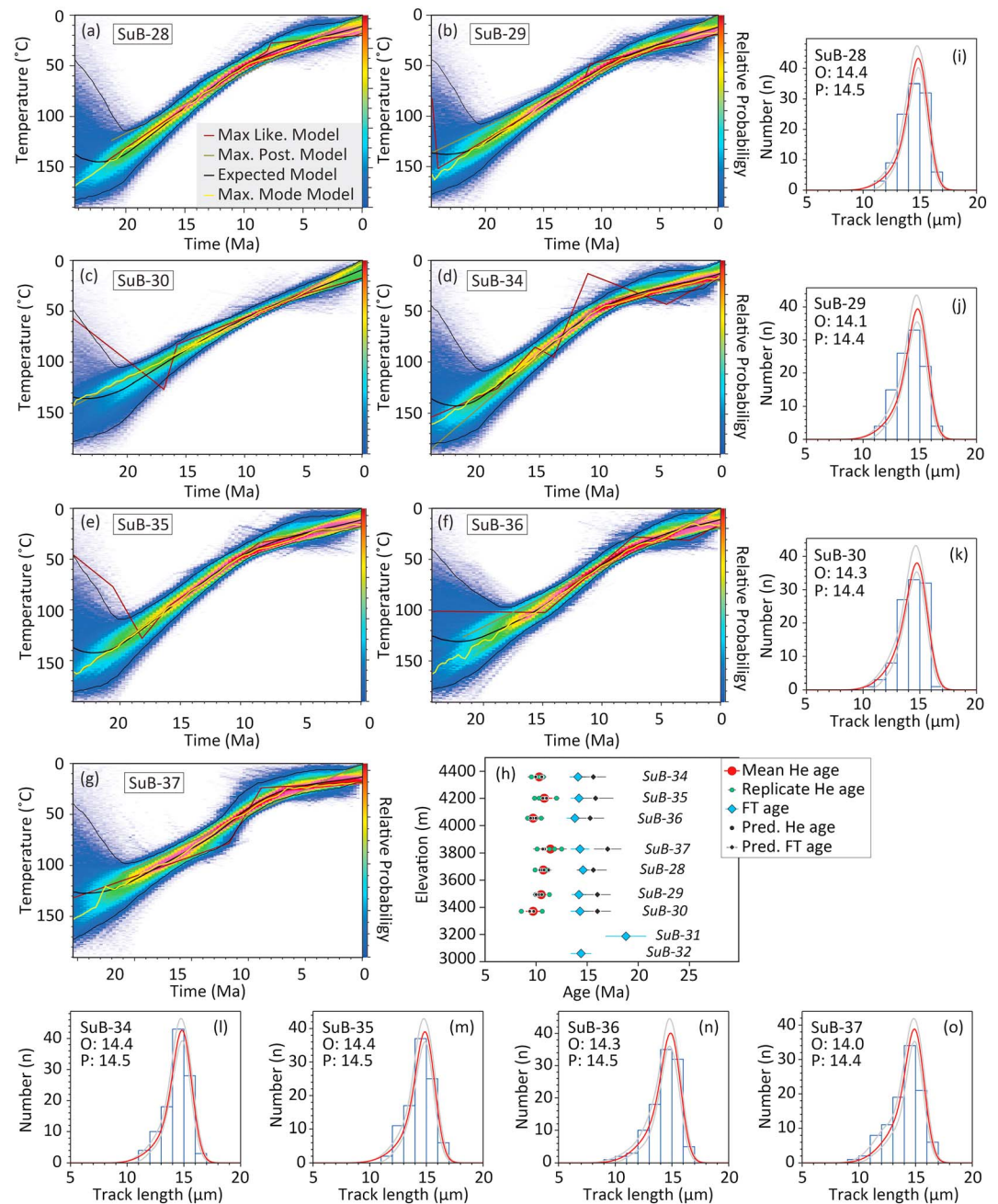
Figure 8. (a–g) QTQt thermal history inversions for Transect 3. Thin black lines show the 95% credible intervals of the expected model. (h) Comparison between observed and predicted age-elevation distribution. All the predicted AHe and apatite fission track ages are from the expected model. (i–o) Comparison between observed (o) and predicted (p) projected fission track length.

we derive an exhumation rate of 0.4 ± 0.2 km/Ma during this period. This is consistent with the exhumation rate of 0.1–0.3 km/Ma based on the observed age-elevation relationships (Figure 5c). Furthermore, assuming a closure temperature of 60 °C for AHe and 110 °C for AFT, an average surface temperature of 10 °C, and a geothermal gradient of 20–25 °C/km, we derive a long-term average exhumation rate of 0.2–0.3 km/Ma for the samples in Transect 2 since ~14–16 Ma. This exhumation rate coincides with that obtained from the age-elevation relationship during ~16 and 9 Ma, suggesting that the samples in Transect 2 may have experienced monotonic cooling with a consistent exhumation rate since at least 14–16 Ma.

Our AFT ages from Transects 2 and 3 as well as sample SuB-05 from Transect 1 all fall in a narrow 14–16 Ma range (Table 1). All these samples also have long (>13.5 μm) mean track lengths, implying rapid cooling through the fission track annealing temperature. This means that the western Danghenan Shan has experienced rapid exhumation since at least 14–16 Ma. QTQt modeling for all these samples also indicates monotonic cooling since 15–20 Ma with an approximately constant cooling rate of ~5–6 °C/Ma. Furthermore, in Transect 1, sample SuB-05-2, which lies just ~900 m to the north of SuB-05, has a younger AHe age of 9.5 ± 1.9 Ma, but a much older AFT age of 24.1 ± 1.3 Ma. Compared to the 14.6 Ma difference between AFT and AHe ages for SuB-05-2, the 6.3 Ma age difference for SuB-05 indicates a transition to relatively rapid exhumation between 24.1 ± 1.3 and 14.97 ± 0.89 Ma (Figure 5b and Table 1). Similarly, SuB-05-4 has an AHe age of 9.7 ± 1.1 Ma and an AFT age of 18.8 ± 1.0 Ma, which is also consistent with accelerated exhumation between 18.8 ± 1.0 and 14.97 ± 0.89 Ma.

The AFT ages of Transect 1 suggest a systematic southward increase of exhumation since the early Cenozoic (Figure 5b). We attribute this trend to northward tilting of the hanging wall. This is supported by field observations and satellite imagery (Google Earth), which reveal a pronounced topographic asymmetry in the western Danghenan Shan. In the adjacent area of Transect 1, the northern flank of the mountain range is gentler than its southern one and the mountain ridge is significantly biased toward the south. The thrust fault along the southern range front is continuous and is visible as a linear feature on the satellite imagery, whereas the northern mountain range front is irregular and sinuous (Figure 3a). Figure 5a shows a schematic structural model of Transect 1, which shows increasing exhumation toward F1 that controlled by the displacement along the fault. Figure 5b shows AFT and AHe ages plotted versus distance from F1 along a N-S azimuth perpendicular to the trend of F1 and the mountain range. Most AHe ages along this transect fall in the range of 9–12 Ma except for the northernmost sample SuB-07, which has an AHe age of 20.8 ± 3.8 Ma. The narrow range and excellent reproducibility of the AHe data tightly constrains the timing of the thrust faulting. In contrast, AFT ages increase nearly monotonically from 14.97 ± 0.89 Ma near F1 to 58.5 ± 1.6 Ma at ~5.7 km distance from F1 (excluding sample SuB-05-2). Assuming a single tilted block model for Transect 1, the monotonic and significant dispersion of the AFT ages suggests a steady cooling from the early Cenozoic (~58.5 Ma) to middle Miocene (~15 Ma) with relatively slow rate. The inverse modeling of samples SuB-06 and SuB-07 yields a similar thermal history including ~60–80 °C of rapid cooling starting ~16–20 Ma after a prolonged period of isothermal holding since at least the early Cenozoic. Bearing in mind the age-elevation profile of Transect 2 that shows the rapid exhumation began at least since 14–16 Ma, we tightly constrain the initial timing of rapid exhumation in the western Danghenan Shan to be ~15 Ma.

Vertical age-elevation profiles are usually interpreted to mark the onset of rapid cooling (Gleadow et al., 1986). Transect 3 features constant AFT and AHe ages of ca. 14 Ma and ca. 10.6 Ma, respectively (Figure 5d). Transect 3 can be divided into two elevation profiles that separated by the mountain ridge. The southern profile with four samples was collected within 2 km to F1, whereas the northern one was collected within 2.5 km to F2. The uniform AFT ages for both the northern and southern elevation profiles indicate that the thrust faults (F1 and F2) bounding the western Danghenan Shan have undergone rapid slip since or slightly earlier than ~14 Ma. However, the ~4 Ma difference between the AFT and AHe ages is similar to that in Transect 2, suggesting that both transects may have experienced a similar exhumation rate between ~14 and 10.6 Ma. Thus, the almost vertical age-elevation relationship in Transect 3 may indicate that these samples were located at the same crustal depth when they passed through the AFT and AHe closure temperatures and subsequently underwent structural deformation. In other words, upper crustal folding exposed these samples to the current localities with different elevations because of unequal uplift rates. Combining the thermochronological data in Transects 2 and 3, we argue for a holistic interpretation for all the AFT and AHe ages. Under this model, all the samples underwent exhumation at a constant rate of 0.1–0.3 km/Ma from ~16 until 9 Ma. Then, N-S convergence induced an anticlinal folding, increasing uplift rates for the samples close to the anticline axis.

5.2. Tectonic Implications

5.2.1. Implications for Slip of the Altyn Tagh Fault

The Qilian Shan is dominated by active crustal shortening (e.g., Burchfiel et al., 1989; Meyer et al., 1998; Tapponnier & Molnar, 1977). The active thrusts at the western end of the Qilian Shan terminate at the

Altyn Tagh fault and are not truncated or offset by it, but branch from it. This fault geometry and kinematics indicate that the active thrusting at the western end of the Qilian Shan is related to strike-slip motion along the Altyn Tagh fault (e.g., Meyer et al., 1998; Yin et al., 2002). Different models have been proposed to predict the relative initial timing of thrusting in the Qilian Shan and left-lateral slip along the Altyn Tagh fault. Yue and Liou (1999) proposed a two-stage evolution model suggesting that the Altyn Tagh fault extended northeastward along the Alxa-East Mongolia fault and was dominated by strike slip at the first stage; then during the second stage, the Alxa-East Mongolia fault became inactive and the left slip along the Altyn Tagh fault has been accommodated by shortening of the Qilian Shan and Qaidam Basin since the middle Miocene (~13–16 Ma). By analyzing provenance of conglomerate in the NW Qaidam Basin, Wu, Xiao, Yang, et al. (2012) also proposed a two-stage evolution model for the Altyn Tagh fault: (1) Altyn Tagh fault was a basal shear zone confined in the middle-lower crust during the first stage of ~36–15 Ma; (2) crust beneath the Altyn Mountain was split and left-slip movement initiated at ~15 Ma. Based on magnetostratigraphic analysis results in the western Hexi Corridor and previous studies, W. Wang, Zhang, Pang, et al. (2016) proposed a two-stage northward propagated model of the Altyn Tagh fault, in which the fault terminated in the western Qaidam Basin in Eocene–Oligocene, then it propagated to the northeast to its present eastern end by ~13 Ma. In this model, the intensive crustal shortening and rapid growth of the Qilian Shan has initiated since the middle Miocene. Using high-resolution seismic reflection data from the northwestern margin of the Qaidam Basin, Wu et al. (2019) suggest a three-stage deformation history for the Altyn Tagh fault. The fault was characterized by small magnitudes of strain with nearly constant rates during the first stage of ~53.5–16.9 Ma; strain rates increased and the local unconformity along the Altyn Tagh fault was developed in the second stage of ~16.9–15.3 Ma; strain rates dropped abruptly by 1 or 2 orders of magnitude in the third stage of 15.3 Ma to present. In this model, the south Qilian Shan may uplift in early Cenozoic (~53.5 Ma). Based on fault geometry and kinematics on both side of the Altyn Tagh fault, Yin et al. (2002) proposed four possible temporal relationships between the movements on the Altyn Tagh fault and thrusting at the western end of the Qilian Shan. They postdate that the Altyn Tagh fault has been active since ~49 Ma in the Qimen Tagh and until ~33 Ma in the Danghenan Shan region. However, these models have been difficult to test due to a lack of unequivocal chronological constrains.

The thrusting and crustal shortening in the western Danghenan Shan are intimately related to the sinistral slip along the Altyn Tagh fault (Burchfiel et al., 1989; Meyer et al., 1998; Yin et al., 2002). This is supported by the present fault geometry in the western Danghenan Shan. The thrust fault along the southern range front of the Danghenan Shan is oriented along an E-W direction in our study area and veers by ~20° counterclockwise toward the Altyn Tagh fault (Figure 2). The fault can be traced from the south of the Aksay Bend until Transect 2 and extends even further eastward. The fault geometry suggests that the thrust fault along the southern Danghenan Shan is not truncated by the Altyn Tagh fault, but branches from it. Our new thermochronological data suggest that the western Danghenan Shan began to rise in the middle Miocene. This means that the left-lateral slip motion has been transferred to crustal shortening in the Qilian Shan since then. Thus, the Altyn Tagh fault in the Qilian Shan must have been active since at least the middle Miocene (~15 Ma). Relatively slow exhumation in the Danghenan Shan between the early Cenozoic and late Oligocene revealed by AFT data in Transect 1 may be related to the early Cenozoic deformation exhumation in the Danghenan Shan region (Jolivet et al., 2001; Sobel et al., 2001), whereas the exhumation rate in the early Cenozoic must be much lower than that since the middle Miocene derived from this study. The relatively slow exhumation before the late Oligocene supports fast and concentrated slip along the Altyn Tagh fault in the early stage (Yue & Liou, 1999), or, alternatively, a relatively quiescent period before the middle Miocene for its northeastern section (e.g., E. Wang, 1997; Sun et al., 2005; Wu, Xiao, Yang, et al., 2012; Wang, Zhang, Pang, et al., 2016).

The Subei Basin is at the western end of the Danghenan Shan such that its depositional history will provide insight into the deformation timing of the Danghenan Shan and Altyn Tagh fault. Gilder et al. (2001) measured a paleomagnetic section in Xishuigou from ~26.1 to 18.8 Ma and magnetic parameters suggest rapid uplift occurred at ~21 Ma. Yin et al. (2002) constrained magnetostratigraphy of the same section from ~33 to 27 Ma and they considered the initiation of deposition as the onset timing of uplift of the Danghenan Shan (~33 Ma). Due to lack of direct fossil evidence found in their field investigations, the correlations to the standard polarity time scale are not unique. X. Wang et al. (2003) reinterpreted these published data to a span of 20–9.3 Ma based on detailed paleontologic evidence. They estimated the Danghenan Shan

began to uplift from 12 to 9 Ma based on the initiation of coarse sediments in the section. To the west of this section by ~5 km, Sun et al. (2005) provided magnetogtratigraphy in the Tiejianggou section, which has similar sedimentary sequence with the Xishuigou section, to a span of 22.8–9 Ma. They indicate that coarse conglomerates began to accumulate and magnetic susceptibility increased after ~13.7 Ma, which is attributed to the tectonic uplift around the western Danghenan Shan. They also suggest that the fine-textured mudstone with horizontal bedding accumulated between the late Oligocene and early Miocene represents lacustrine environment and distal source deposit, which means that the region near the western Danghenan Shan was large low-relief basin without mountains to provide high-energy alluvial or fluvial sediments into the Subei Basin during that time. Furthermore, Lin et al. (2015) reported a distinct change in slope of the peak age and lag time of the detrital apatite fission track occurred at ~14 Ma in the Tiejianggou section, which is interpreted as a provenance change caused by the uplift of the western Danghenan Shan. Therefore, combining the evidence of magnetogtratigraphy, paleontology, lithofacies, initiation of coarse sediment, and provenance change with our thermochronological results, we prefer to suggest that the Altyn Tagh fault in the Subei Basin was reactivated since the middle Miocene.

The proposed rapid exhumation commencing in the middle Miocene coincides with the onset of a suite of significant phenomena along the Altyn Tagh fault: (1) thermochronology on basement rocks along the Altyn Tagh fault (e.g., Jolivet et al., 1999, 2001; Ritts et al., 2008; Shi et al., 2018; Sobel et al., 2001; Zhuang et al., 2018); (2) acceleration in sedimentation rate, provenance change and growth strata recorded by paleomagnetic studies in the western Qaidam Basin and along the Altyn Tagh fault (e.g., Chang et al., 2015; Gilder et al., 2001; B. Li et al., 2017; Lu et al., 2014; Wang, Zhang, Pang, et al., 2016; W. Zhang et al., 2013); (3) provenance analyses based on lithofacies variations and detrital zircon U–Pb ages along the Altyn Tagh fault (e.g., F. Cheng et al., 2015, 2016; Wu, Xiao, Wang, et al., 2012; Wu, Xiao, Yang, et al., 2012; Yue et al., 2001; Zhu et al., 2017; T. Zhang et al., 2018); and (4) initiation of growth strata in the basins along the Altyn Tagh fault and western Qaidam Basin revealed by seismic data (e.g., F. Cheng et al., 2014, 2015, 2016; B. Li et al., 2017; R. Liu, Allen, et al., 2017; Yin et al., 2008).

5.2.2. Implications for Building the Northern Tibetan Plateau

Our new thermochronological data combined with published data in the western Danghenan Shan indicate a period of accelerated deformation since the middle Miocene in the southwestern portion of the Qilian Shan. The accelerated deformation in the middle Miocene is observed not only in the southwestern portion of the Qilian Shan but also throughout the rest of the Qilian Shan: (1) Thermochronological data indicate that the northern margin of the Qilian Shan has undergone accelerated exhumation since ~10 Ma (George et al., 2001; B. Li et al., 2019; Zheng et al., 2010, 2017; Zhuang et al., 2018); (2) a shift in provenance in the Hexi Corridor from the Bei Shan to the north to the northern Qilian Shan to the south, and facies change in the Hexi Corridor suggest that the deformation that created the high topography of the northern Qilian Shan began at the middle Miocene (Bovet et al., 2009; Wang, Zhang, Pang, et al., 2016); (3) rapid exhumation of the central Qilian Shan is reported to have occurred since the middle Miocene (Duvall et al., 2013; D. Yuan et al., 2011, 2013; Yu et al., 2019; Zheng et al., 2017); (4) accelerated exhumation and depositional rates, sediment coarsening, development of growth strata, and climate change attributed to mountain building in the middle Miocene are widespread across the eastern portion of the Qilian Shan east of the Qinghai Lake, such as the Linxia, Xunhua, Guide, and Gonghe basins (see a review in Lease, 2014); and (5) new thermochronological data and magnetostratigraphy in the southern margin of the Qilian Shan and northern Qaidam Basin suggest that the region has experienced rapid exhumation since the middle Miocene (Fang et al., 2007; Pang et al., 2019; W. Wang, Zheng, Zhang, et al., 2017; Zhuang et al., 2018; Figure 9a).

The widespread middle Miocene deformation across the entire Qilian Shan is apparently incompatible with the stepwise northward growth model for north Tibet, which suggests that the crustal shortening related to the India-Eurasia collision and postcollision convergence has propagated into the southern Qilian Shan in the Paleocene or early Eocene then extended northward progressively (e.g., Bovet et al., 2009; Qi et al., 2016). However, the geodynamics caused the widespread middle Miocene deformation in north Tibet remains poorly understood. It may be due to a large increase in horizontal compressive force in response to the removal of overthickened, unstable mantle lithosphere in the southern-central Tibetan Plateau (Molnar & Stock, 2009), continued northward propagated crustal shortening since the India-Eurasia collision (England & Houseman, 1986), a significant amount of extrusion transferred from the Altyn Tagh
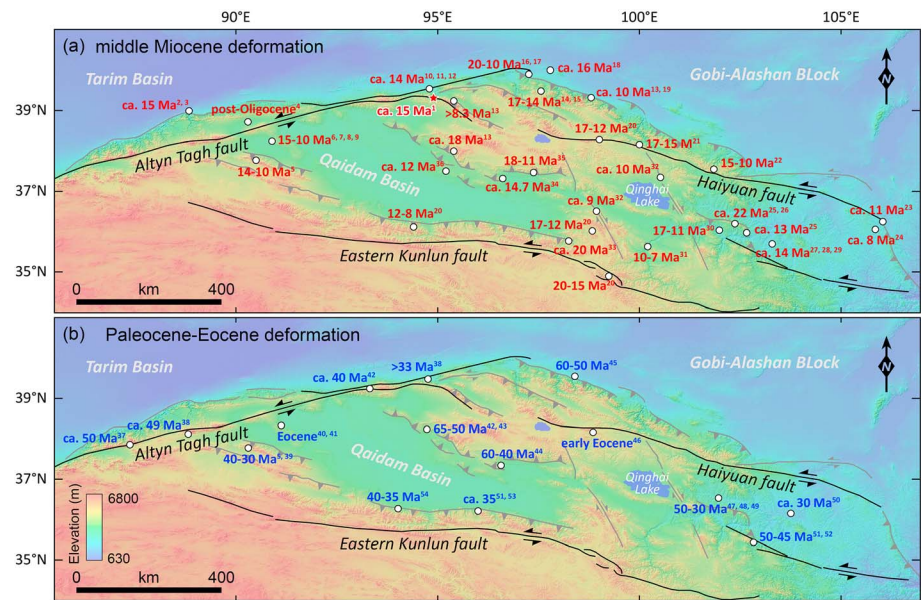
Figure 9. Topographic map of north Tibet with major faults and initial deformation timing in (a) middle Miocene and (b) Paleocene to Eocene. Initiation ages were derived from: 1—This study; 2—Ritts et al. (2008); 3—Shi et al. (2018); 4—Yue and Liou (1999); 5—Y. Wang et al. (2018); 6—R. Liu, Allen, et al. (2017); 7—Chang et al. (2015); 8—B. Li et al. (2017); 9—Cheng et al. (2015); 10—X. Wang et al. (2003); 11—Sun et al. (2005); 12—Lin et al. (2015); 13—Zhuang et al. (2018); 14—D. Yuan et al. (2013); 15—Zheng et al. (2017); 16—Bovet et al. (2009); 17—George et al. (2001); 18—Wang, Zhang, Pang, et al. (2016); 19—Zheng et al. (2010); 20—Duvall et al. (2013); 21—Yu et al. (2019); 22—B. Li et al. (2019); 23—W. Wang et al. (2011); 24—Zheng et al. (2006); 25—Lease et al. (2011); 26—Lease et al. (2012); 27—Fang et al. (2003); 28—Garzione et al. (2005); 29—Hough et al. (2011); 30—Yan et al. (2006); 31—Craddock et al. (2011); 32—D. Yuan et al. (2011); 33—W. Yuan et al. (2006); 34—Fang et al. (2007); 35—Pang et al. (2019); 36—W. Wang, Zheng, Zhang, et al. (2017); 37—Jolivet et al., 1999; 38—Yin et al. (2002); 39—D. Liu, Li, et al. (2017); 40—F. Cheng et al. (2015); 41—F. Cheng et al. (2016); 42—Jolivet et al. (2001); 43—Yin et al. (2008); 44—He et al. (2018); 45—He et al. (2017); 46—Qi et al. (2016); 47—Dupont-Nivet et al. (2004); 48—Dai et al. (2006); 49—J. Zhang et al. (2015); 50—Wang, Zhang, Liu, et al. (2016); 51—Clark et al. (2010); 52—Duvall et al. (2011); 53—Mock et al. (1999); 54—F. Wang, Shi, et al. (2017).

fault to distributed shortening in the Qilian Shan (Yue et al., 2001; Yue & Liou, 1999), or change in the external boundary condition between the Asia and Pacific (Zhuang et al., 2018).

Early Cenozoic deformation was reported in north Tibet, such as in the Qimen Tagh, southern and northern margins of the Qaidam Basin, western Qinling, and Xining-Lanzhou Basin (e.g., Clark et al., 2010; Cheng et al., 2015, 2016; Dai et al., 2006; Dupont-Nivet et al., 2004; Duvall et al., 2011; Jolivet et al., 2001; Mock et al., 1999; F. Qi et al., 2016; Zhuang et al., 2011; W. Wang, Zhang, Liu, et al., 2016; F. Wang, Shi, et al., 2017; Yin et al., 2002, 2008; Zhang et al., 2015; Figure 9b). A major part of the evidence for the early Cenozoic deformation come from the depositional history in the Qaidam Basin. However, the age of the Lulehe formation, which marks the initiation of Cenozoic sedimentation in the Qaidam basin, remains highly debated. It was considered that the Lulehe formation was deposited during Paleocene and early Eocene (~50 Ma) based on magnetostratigraphy, spore and pollen assemblages, and regional lithostratigraphic correction (e.g., GBGMR, 1989; F. Cheng et al., 2018; Fang et al., 2007; Yin et al., 2008). If this traditional age model is correct, the northern and southern margins of the Qaidam Basin have received sediments from the adjacent mountains, such as the southern Qilian Shan and/or eastern Kunlun Shan in the early Cenozoic, which may derive from tectonic exhumation then. This is supported by thermochronological data in the Qimen Tagh (Jolivet et al., 1999; D. Liu, Li, et al., 2017; Y. Wang et al., 2018), eastern Kunlun Shan (Clark et al., 2010; Mock et al., 1999; F. Wang, Shi, et al., 2017), and northern margin of the Qaidam Basin (He et al., 2018; Jolivet et al., 2001), and estimation on the sediments preserved in the Qaidam Basin and materials eroded in the surrounding drainage area (Cheng et al., 2018). However, recent published magnetostratigraphy and mammalian biostratigraphy refine the onset of basin fill in the Qaidam Basin to ~25.5 Ma and reveal that the detritus shed from the southern Qilian Shan occurred at ~12 Ma, suggesting that the deformation in the southern Qilian Shan is significantly later than previously

estimated (W. Wang, Zheng, Zhang, et al., 2017). It is consistent with thermochronological data along the mountain ranges in the southern margin of the Qilian Shan, which has undergone a phase of accelerated exhumation since the early-middle Miocene (Pang et al., 2019; Zhuang et al., 2018). It is also supported by provenance analyses for the Qaidam Basin, which indicate that early Cenozoic sediments in the northern Qaidam Basin were shed from the Kunlun Shan rather than the southern Qilian Shan, and provenance change occurred during early-middle Miocene (Bush et al., 2016; W. Wang, Zheng, Zhang, et al., 2017). While Lu et al. (2018) suggest that Bush et al. (2016) may misidentify the underlying Cretaceous Quanyagou formation as the lower part of the Lulehe formation such that produce improper conclusions, they concluded that the Lulehe formation is characterized by proximal alluvial fan deposits that originated from the northern Qaidam Basin and the southern Qilian Shan based on evidence of sedimentology, facies analysis, and seismic reflection profiles (e.g., F. Cheng et al., 2019; Lu et al., 2018; Yin et al., 2008). Cheng et al. (2018) suggest that if both the traditional (~50 Ma) and younger (~25.5 Ma) age models are correct, the Qaidam Basin may experience diachronous basin-fill process and the lithostratigraphic units throughout the basin are time transgressive. The debates on the age and provenance of the Lulehe formation highlight the need for further effort to determine the depositional age of the strata in the Qaidam Basin and more robust thermochronological data to reveal the exhumation histories of the southern Qilian Shan and eastern Kunlun Shan. Some other evidence for the early Cenozoic deformation derive from single-sample modeling of low-temperature thermochornological data (e.g., Jolivet et al., 2001; D. Liu, Li, et al., 2017; Mock et al., 1999; Qi et al., 2016; J. Zhang et al., 2017). However, thermal history modeling, especially for single sample, may just provide one possible but not unique cooling history to produce the age and length distribution due to variation on reproducibility of fission track length data, data entry, model setup, and modeling software approach (Ketcham et al., 2009, 2018). It strongly highlights the importance of collecting thermochronological samples systematically, such as along elevation profiles or based on tectonic deformation patterns.

Compared with the widespread middle Miocene deformation across the entire Qilian Shan, the early Cenozoic deformation is just reported south of the Qaidam Basin (e.g., Clark et al., 2010; Jolivet et al., 1999, 2001; D. Liu, Li, et al., 2017; Mock et al., 1999; F. Wang, Shi, et al., 2017; Y. Wang et al., 2018; Yin et al., 2002), the northern Qaidam Basin (e.g., F. Cheng et al., 2019; He et al., 2018; Jolivet et al., 2001; Lu et al., 2018; Yin et al., 2008; Zhuang et al., 2011), and parts of the Qilian Shan, such as the Xining-Lanzhou Basin (Dupont-Nivet et al., 2004; Dai et al., 2006; J. Zhang et al., 2015; Wang, Zhang, Liu, et al., 2016), western Qinling (Clark et al., 2010; Duvall et al., 2011), and the central-northern Qilian Shan (e.g., Qi et al., 2016; He et al., 2017; Figure 9b). The Paleocene-Eocene and widespread middle Miocene deformation suggest that the crustal shortening has extended into the northern Tibetan Plateau to reactive preexisting weaknesses shortly after the India-Eurasia collision, followed by a phase of extensive crustal shortening across the Qilian Shan since the middle Miocene. The present tectonic configuration and topography in the Qilian Shan were likely established since the middle Miocene. Furthermore, as the Paleocene-Eocene deformation and relatively high paleoelevation have been widely observed in the southern and central Tibetan Plateau, such as the Lhasa, Qiangtang, and Hoh Xil (Horton et al., 2002; C. Wang et al., 2014), the eastern Kunlun Shan may act as the northern frontier of the high-topographic plateau before the middle Miocene and the preexisting weaknesses to the north of the Kunlun Shan, such as the northern Qaidam Basin and western Qinling, may have been reactivated during the period. Then a phase of distributed crustal shortening extended to the farther north into the Qilian Shan. This model is consistent with the two phase of deformation model for the Altyn Tagh fault, which suggests that the southwestern section of the Altyn Tagh fault was initiated during the Oligocene (>30 Ma) and the fault propagated to its eastern section during the middle Miocene (Wang, Zhang, Pang, et al., 2016). It is also supported by our new thermochronological data combined with published depositional results in the Subei Basin (Lin et al., 2015; Sun et al., 2005; X. Wang et al., 2003), which suggest that the Altyn Tagh fault in the Subei Basin has experienced accelerated deformation since the middle Miocene.

6. Conclusions

The new AFT and AHe data from the western Danghenan Shan in north Tibet provide new temporal constraints on the deformation of the southwestern portion of the Qilian Shan and the Altyn Tagh fault system. The age-elevation relationships and AFT/AHe lag times indicate an average exhumation rate of

0.1–0.3 km/Ma from ~16 to 9 Ma for the western Danghenan Shan. The AFT/AHe ages and thermal history modeling indicate that accelerated exhumation initiated in the middle Miocene, more likely ~15 Ma. Regional geology suggests that the exhumation was mainly controlled by the thrust fault along the southern range front of the western Danghenan Shan, which is a branch of the Altyn Tagh fault. Thus, we conclude that the left-slip motion along the Altyn Tagh fault has been transferred to crustal shortening in the Qilian Shan since at least the middle Miocene.

References

An, Z. S., Kutzbach, J. E., Prell, W. L., & Porter, S. C. (2001). Evolution of Asian monsoons and phased uplift of the Himalaya–Tibetan plateau since Late Miocene times. *Nature*, *411*(6833), 62.

Bohlin, B. (1937). Oberoligozäne Säugetiere aus dem Shargaltein-Tal (Western Kansu). *Palaeontologica Sinica, New Series C* (Vol. *3*, pp. 1–66).

Bovet, P. M., Ritts, B. D., Gehrels, G., Abbink, A. O., Darby, B., & Hourigan, J. (2009). Evidence of Miocene crustal shortening in the north Qilian Shan from Cenozoic stratigraphy of the western Hexi Corridor, Gansu Province, China. *American Journal of Science*, *309*(4), 290–329. https://doi.org/10.2475/00.4009.02

Burchfiel, B. C., Deng, Q. D., Molnar, P., Royden, L., Wang, Y. P., Zheng, P. Z., & Zhang, W. Q. (1989). Intracrustal detachment within zones of continental deformation. *Geology*, *17*, 748–752. https://doi.org/10.1130/0091-7613(1989)017<0448:IDWZOC>2.3.CO;2

Bush, M. A., Saylor, J. E., Horton, B. K., & Nie, J. (2016). Growth of the Qaidam Basin during Cenozoic exhumation in the northern Tibetan Plateau: Inferences from depositional patterns and multiproxy detrital provenance signatures. *Lithosphere*, *8*(1), 58–82. https://doi.org/10.1130/L449.1

Chang, H., Li, L., Qiang, X., Garzione, C. N., Pullen, A., & An, Z. (2015). Magnetostratigraphy of Cenozoic deposits in the western Qaidam Basin and its implication for the surface uplift of the northeastern margin of the Tibetan Plateau. *Earth and Planetary Science Letters*, *430*, 271–283. https://doi.org/10.1016/j.epsl.2015.08.029

Cheng, F., Garzione, C., Jolivet, M., Guo, Z., Zhang, D., & Zhang, C. (2018). A new sediment accumulation model of Cenozoic depositional ages from the Qaidam basin, Tibetan Plateau. *Journal of Geophysical Research: Earth Surface*, *123*, 3101–3121. https://doi.org/10.1029/2018JF004645

Cheng, F., Garzione, C. N., Jolivet, M., Guo, Z., Zhang, D., Zhang, C., & Zhang, Q. (2019). Initial deformation of the northern Tibetan plateau: insights from deposition of the Lulehe Formation in the Qaidam Basin. *Tectonics*, *38*, 741–766. https://doi.org/10.1029/2018TC005214

Cheng, F., Guo, Z., Jenkins, H. S., Fu, S., & Cheng, X. (2015). Initial rupture and displacement on the Altyn Tagh fault, northern Tibetan Plateau: Constraints based on residual Mesozoic to Cenozoic strata in the western Qaidam Basin. *Geosphere*, *11*(3), 921–942. https://doi.org/10.1130/GES01070.1

Cheng, F., Jolivet, M., Fu, S., Zhang, C., Zhang, Q., & Guo, Z. (2016). Large-scale displacement along the Altyn Tagh Fault (North Tibet) since its Eocene initiation: Insight from detrital zircon U–Pb geochronology and subsurface data. *Tectonophysics*, *677-678*, 261–279. https://doi.org/10.1016/j.tecto.2016.04.023

Cheng, F., Jolivet, M., Fu, S., Zhang, Q., Guan, S., Yu, X., & Guo, Z. (2014). Northward growth of the Qimen Tagh Range: A new model accounting for the late Neogene strike-slip deformation of the SW Qaidam Basin. *Tectonophysics*, *632*, 32–47. https://doi.org/10.1016/j.tecto.2014.05.034

Clark, M. K. (2012). Continental collision slowing due to viscous mantle lithosphere rather than topography. *Nature*, *483*(7387), 74–77. https://doi.org/10.1038/nature10848

Clark, M. K., Farley, K. A., Zheng, D., Wang, Z., & Duvall, A. R. (2010). Early Cenozoic faulting of the northern Tibetan Plateau margin from apatite (U–Th)/He ages. *Earth and Planetary Science Letters*, *296*(1–2), 78–88. https://doi.org/10.1016/j.epsl.2010.04.051

Cowgill, E., Yin, A., Harrison, T. M., & Xiao-Feng, W. (2003). Reconstruction of the Altyn Tagh fault based on U-Pb geochronology: Role of back thrusts, mantle sutures, and heterogeneous crustal strength in forming the Tibetan Plateau. *Journal of Geophysical Research*, *108*(B7), 2346. https://doi.org/10.1029/2002JB002080

Craddock, W., Kirby, E., & Zhang, H. (2011). Late Miocene–Pliocene range growth in the interior of the northeastern Tibetan Plateau. *Lithosphere*, *3*(6), 420–438. https://doi.org/10.1130/L159.1

Dai, S., Fang, X., Dupont-Nivet, G., Song, C., Gao, J., Krijgsman, W., et al. (2006). Magnetostratigraphy of Cenozoic sediments from the Xining Basin: Tectonic implications for the northeastern Tibetan Plateau. *Journal of Geophysical Research*, *111*, B11102. https://doi.org/10.1029/2005JB004187

Donelick, R. A., Ketcham, R. A., & Carlson, W. D. (1999). Variability of apatite fission track annealing kinetics: II. Crystallographic orientation effects. *American Mineralogist*, *84*(9), 1224–1234. https://doi.org/10.2138/am-1999-0902

Donelick, R. A., & Miller, D. S. (1991). Enhanced TINT fission track densities in low spontaneous track density apatites using 252Cf-derived fission fragment tracks: A model and experimental observations. *International Journal of Radiation Applications and Instrumentation. Part D. Nuclear Tracks and Radiation Measurements*, *18*(3), 301–307. https://doi.org/10.1016/1359-0189(91)90022-A

Dupont-Nivet, G., Horton, B. K., Butler, R. F., Wang, J., Zhou, J., & Waanders, G. L. (2004). Paleogene clockwise tectonic rotation of the Xining-Lanzhou region, northeastern Tibetan Plateau. *Journal of Geophysical Research*, *109*, B04401. https://doi.org/10.1029/2003JB002620

Duvall, A. R., Clark, M. K., Kirby, E., Farley, K. A., Craddock, W. H., Li, C., & Yuan, D. Y. (2013). Low-temperature thermochronometry along the Kunlun and Haiyuan Faults, NE Tibetan Plateau: Evidence for kinematic change during late-stage orogenesis. *Tectonics*, *32*, 1190–1211. https://doi.org/10.1002/tect.20072

Duvall, A. R., Clark, M. K., van der Pluijm, B. A., & Li, C. (2011). Direct dating of Eocene reverse faulting in northeastern Tibet using Ar-dating of fault clays and low-temperature thermochronometry. *Earth and Planetary Science Letters*, *304*(3–4), 520–526. https://doi.org/10.1016/j.epsl.2011.02.028

Ehlers, T. A., Chaudhri, T., Kumar, S., Fuller, C. W., Willett, S. D., Ketcham, R. A., et al. (2005). Computational tools for low-temperature thermochronometer interpretation. *Reviews in Mineralogy and Geochemistry*, *58*(1), 589–622. https://doi.org/10.2138/rmg.2005.58.22

England, P., & Houseman, G. (1986). Finite strain calculations of continental deformation: 2Comparison with the India-Asia collision zone. *Journal of Geophysical Research*, *91*(B3), 3664–3676. https://doi.org/10.1029/JB091iB03p03664

Fang, X., Garzione, C., Van der Voo, R., Li, J., & Fan, M. (2003). Flexural subsidence by 29 Ma on the NE edge of Tibet from the magnetostratigraphy of Linxia Basin, China. *Earth and Planetary Science Letters*, *210*(3–4), 545–560. https://doi.org/10.1016/S0012-821X(03)00142-0

Fang, X., Zhang, W., Meng, Q., Gao, J., Wang, X., King, J., et al. (2007). High-resolution magnetostratigraphy of the Neogene Huaitoutala section in the eastern Qaidam Basin on the NE Tibetan Plateau, Qinghai Province, China and its implication on tectonic uplift of the NE Tibetan Plateau. *Earth and Planetary Science Letters*, *258*(1–2), 293–306. https://doi.org/10.1016/j.epsl.2007.03.042

Farley, K. A. (2000). Helium diffusion from apatite: General behavior as illustrated by Durango fluorapatite. *Journal of Geophysical Research*, *105*(B2), 2903–2914. https://doi.org/10.1029/1999JB900348

Farley, K. A., & Stockli, D. F. (2002). (U-Th)/He dating of phosphates: Apatite, monazite, and xenotime. *Reviews in Mineralogy and Geochemistry*, *48*(1), 559–577. https://doi.org/10.2138/rmg.2002.48.15

Flowers, R. M., Ketcham, R. A., Shuster, D. L., & Farley, K. A. (2009). Apatite (U-Th)/He thermochronometry using a radiation damage accumulation and annealing model. *Geochimica et Cosmochimica Acta*, *73*(8), 2347–2365. https://doi.org/10.1016/j.gca.2009.01.015

Gallagher, K. (2012). Transdimensional inverse thermal history modeling for quantitative thermochronology. *Journal of Geophysical Research*, *117*, B02408. https://doi.org/10.1029/2011JB008825

Gansu Bureau of Geology and Mineral Resources (GBGMR) (1989). *Regional Geology of Gansu Province (in Chinese with English abstract)* (pp. 120–137). Beijing: Geological Publishing House.

Garzione, C. N., Ikari, M. J., & Basu, A. R. (2005). Source of Oligocene to Pliocene sedimentary rocks in the Linxia basin in northeastern Tibet from Nd isotopes: Implications for tectonic forcing of climate. *Geological Society of America Bulletin*, *117*(9), 1156–1166. https://doi.org/10.1130/B25743.1

George, A. D., Marshallsea, S. J., Wyrwoll, K. H., Chen, J., & Lu, Y. (2001). Miocene cooling in the northern Qilian Shan, northeastern margin of the Tibetan Plateau, revealed by apatite fission-track and vitrinite-reflectance analysis. *Geology*, *29*(10), 939–942. https://doi.org/10.1130/0091-7613(2001)029<0939:MCITNQ>2.0.CO;2

Gilder, S., Chen, Y., & Sen, S. (2001). Oligo-Miocene magnetostratigraphy and rock magnetism of the Xishuigou section, Subei (Gansu Province, western China) and implications for shallow inclinations in central Asia. *Journal of Geophysical Research*, *106*(B12), 30,505–30,521. https://doi.org/10.1029/2001JB000325

Gleadow, A., Duddy, I., Green, P. F., & Lovering, J. (1986). Confined fission track lengths in apatite: A diagnostic tool for thermal history analysis. *Contributions to Mineralogy and Petrology*, *94*(4), 405–415. https://doi.org/10.1007/BF00376334

Gleadow, A. J. (1981). Fission-track dating methods: what are the real alternatives? *Nuclear Tracks*, *5*(1–2), 3–14. https://doi.org/10.1016/0191-278X(81)90021-4

Gleadow, A. J., Kohn, B. P., Brown, R. W., O'Sullivan, P. B., & Raza, A. (2002). Fission track thermotectonic imaging of the Australian continent. *Tectonophysics*, *349*(1–4), 5–21. https://doi.org/10.1016/S0040-1951(02)00043-4

Green, P. F., Duddy, I. R., Gleadow, A. J. W., Tingate, P. R., & Laslett, G. M. (1986). Thermal annealing of fission tracks in apatite: 1. A qualitative description. *Chemical Geology: Isotope Geoscience*, *59*, 237–253. https://doi.org/10.1016/0168-9622(86)90074-6

He, P., Song, C., Wang, Y., Meng, Q., Chen, L., Yao, L., et al. (2018). Cenozoic deformation history of the Qilian Shan (northeastern Tibetan Plateau) constrained by detrital apatite fission-track thermochronology in the northeastern Qaidam Basin. *Tectonophysics*, *749*, 1–11. https://doi.org/10.1016/j.tecto.2018.10.017

He, P., Wang, X., Song, C., Wang, Q., Deng, L., & Zhong, S. (2017). Cenozoic evolution of the Western Qinling Mt. Range based on thermochronologic and sedimentary records from the Wudu Basin, NE Tibetan Plateau. *Journal of Asian Earth Sciences*, *138*, 484–494. https://doi.org/10.1016/j.jseaes.2017.02.033

Horton, B. K., Yin, A., Spurlin, M. S., Zhou, J., & Wang, J. (2002). Paleocene–Eocene syncontractional sedimentation in narrow, lacustrine-dominated basins of east-central Tibet. *Geological Society of America Bulletin*, *114*, 771–786. https://doi.org/10.1130/0016-7606(2002)114<0771:PESSIN>2.0.CO;2

Hough, B. G., Garzione, C. N., Wang, Z., Lease, R. O., Burbank, D. W., & Yuan, D. (2011). Stable isotope evidence for topographic growth and basin segmentation: Implications for the evolution of the NE Tibetan Plateau. *Geological Society of America Bulletin*, *123*(1–2), 168–185. https://doi.org/10.1130/B30090.1

Hu, S. B., He, L. J., & Wang, J. Y. (2000). Heat flow in the continental area of China: A new data set. *Earth and Planetary Science Letters*, *179*, 407–419. https://doi.org/10.1016/S0012-821X(00)00126-6

Hurford, A. J., & Green, P. F. (1983). The zeta age calibration of fission-track dating. *Chemical Geology*, *41*, 285–317. https://doi.org/10.1016/S0009-2541(83)80026-6

Jolivet, M., Brunel, M., Roger, F., Tapponnier, P., Arnaud, N., & Seward, D. (1999). Exhumation history of the Altun Shan with evidence for the timing of the subduction of the Tarim block beneath the Altyn Tagh system, North Tibet. *Comptes Rendus de l'Academie des Sciences. Serie 2, Sciences de la Terre et des Planetes*, *329*(10), 749–755.

Jolivet, M., Brunel, M., Seward, D., Xu, Z., Yang, J., Roger, F., et al. (2001). Mesozoic and Cenozoic tectonics of the northern edge of the Tibetan plateau: fission-track constraints. *Tectonophysics*, *343*(1–2), 111–134. https://doi.org/10.1016/S0040-1951(01)00196-2

Ketcham, R. A., Carter, A., Donelick, R. A., Barbarand, J., & Hurford, A. J. (2007). Improved modeling of fission-track annealing in apatite. *American Mineralogist*, *92*(5–6), 799–810. https://doi.org/10.2138/am.2007.2281

Ketcham, R. A., Donelick, R. A., Balestrieri, M. L., & Zattin, M. (2009). Reproducibility of apatite fission-track length data and thermal history reconstruction. *Earth and Planetary Science Letters*, *284*(3–4), 504–515. https://doi.org/10.1016/j.epsl.2009.05.015

Ketcham, R. A., Gautheron, C., & Tassan-Got, L. (2011). Accounting for long alpha-particle stopping distances in (U–Th–Sm)/He geochronology: Refinement of the baseline case. *Geochimica et Cosmochimica Acta*, *75*(24), 7779–7791. https://doi.org/10.1016/j.gca.2011.10.011

Ketcham, R. A., Van Der Beek, P., Barbarand, J., Bernet, M., & Gautheron, C. (2018). Reproducibility of thermal history reconstruction from apatite fission-track and (U-Th)/He data. *Geochemistry, Geophysics, Geosystems*, *19*, 2411–2436. https://doi.org/10.1029/2018GC007555

Lease, R. O. (2014). Cenozoic mountain building on the northeastern Tibetan Plateau. *Geological Society of America Special Papers*, *507*, 115–127. https://doi.org/10.1130/2014.2507(06)

Lease, R. O., Burbank, D. W., Clark, M. K., Farley, K. A., Zheng, D., & Zhang, H. (2011). Middle Mio- cene reorganization of deformation along the northeastern Tibetan Plateau. *Geology*, *39*(4), 359–362. https://doi.org/10.1130/G31356.1

Lease, R. O., Burbank, D. W., Hough, B., Wang, Z., & Yuan, D. (2012). Pulsed Miocene range growth in northeastern Tibet: Insights from Xunhua Basin magnetostratigraphy and provenance. *Geological Society of America Bulletin*, *124*(5–6), 657–677. https://doi.org/10.1130/B30524.1

Li, B., Chen, X., Zuza, A. V., Hu, D., Ding, W., Huang, P., & Xu, S. (2019). Cenozoic cooling history of the North Qilian Shan, northern Tibetan Plateau, and the initiation of the Haiyuan fault: Constraints from apatite-and zircon-fission track thermochronology. *Tectonophysics*, *751*, 109–124. https://doi.org/10.1016/j.tecto.2018.12.005

Li, B., Yan, M., Zhang, W., Fang, X., Meng, Q., Zan, J., et al. (2017). New paleomagnetic constraints on middle Miocene strike-slip faulting along the middle Altyn Tagh Fault. *Journal of Geophysical Research: Solid Earth*, *122*, 4106–4122. https://doi.org/10.1002/2017JB014058

Lin, X., Zheng, D., Sun, J., Windley, B. F., Tian, Z., Gong, Z., & Jia, Y. (2015). Detrital apatite fission track evidence for provenance change in the Subei Basin and implications for the tectonic uplift of the Danghenan Shan (NW China) since the mid-Miocene. *Journal of Asian Earth Sciences*, *111*, 302–311. https://doi.org/10.1016/j.jseaes.2015.07.007

Liu, D., Li, H., Sun, Z., Pan, J., Wang, M., & Wang, H. (2017). AFT dating constrains the Cenozoic uplift of the Qimen Tagh Mountains, Northeast Tibetan Plateau, comparison with LA-ICPMS Zircon U–Pb ages. *Gondwana Research*, *41*, 438–450. https://doi.org/10.1016/j.gr.2015.10.008

Liu, R., Allen, M. B., Zhang, Q., Du, W., Cheng, X., Holdsworth, R. E., & Guo, Z. (2017). Basement controls on deformation during oblique convergence: Transpressive structures in the western Qaidam Basin, northern Tibetan Plateau. *Lithosphere*, *9*(4), L634.1–L634.594. https://doi.org/10.1130/L634.1

Lu, H., Fu, B., Shi, P., Ma, Y., & Li, H. (2016). Constraints on the uplift mechanism of northern Tibet. *Earth and Planetary Science Letters*, *453*, 108–118. https://doi.org/10.1016/j.epsl.2016.08.010

Lu, H., Wang, E., & Meng, K. (2014). Paleomagnetism and anisotropy of magnetic susceptibility of the Tertiary Janggalsay section (southeast Tarim basin): Implications for Miocene tectonic evolution of the Altyn Tagh Range. *Tectonophysics*, *618*, 67–78. https://doi.org/10.1016/j.tecto.2014.01.031

Lu, H., Ye, J., Guo, L., Pan, J., Xiong, S., & Li, H. (2018). Towards a clarification of the provenance of Cenozoic sediments in the northern Qaidam Basin. *Lithosphere*, *11*(2), 252–272. https://doi.org/10.1130/L1037.1

McDowell, F. W., McIntosh, W. C., & Farley, K. A. (2005). A precise 40Ar–39Ar reference age for the Durango apatite (U–Th)/He and fission-track dating standard. *Chemical Geology*, *214*(3–4), 249–263. https://doi.org/10.1016/j.chemgeo.2004.10.002

Meyer, B., Tapponnier, P., Bourjot, L., Metivier, F., Gaudemer, Y., Peltzer, G., et al. (1998). Crustal thickening in Gansu-Qinghai, lithospheric mantle subduction, and oblique, strike-slip controlled growth of the Tibet plateau. *Geophysical Journal International*, *135*(1), 1–47. https://doi.org/10.1046/j.1365-246X.1998.00567.x

Mock, C., Arnaud, N. O., & Cantagrel, J. M. (1999). An early unroofing in northeastern Tibet? Constraints from ^{40}Ar/^{39}Ar thermochronology on granitoids from the eastern Kunlun range (Qianghai, NW China). *Earth and Planetary Science Letters*, *171*(1), 107–122. https://doi.org/10.1016/S0012-821X(99)00133-8

Molnar, P., & Stock, J. M. (2009). Slowing of India's convergence with Eurasia since 20 Ma and its implications for Tibetan mantle dynamics. *Tectonics*, *28*, TC3001. https://doi.org/10.1029/2008TC002271

Molnar, P., & Tapponnier, P. (1977). The collision between India and Eurasia. *Scientific American*, *236*(4), 30–41. https://doi.org/10.1038/scientificamerican0477-30

Pang, J., Yu, J., Zheng, D., Wang, W., Ma, Y., Wang, Y., et al. (2019). Neogene expansion of the Qilian Shan, north Tibet: Implications for the dynamic evolution of the Tibetan Plateau. *Tectonics*, *38*, 1018–1032. https://doi.org/10.1029/2018TC005258

Pang, J., Zheng, D., Ma, Y., Wang, Y., Wu, Y., Wan, J., et al. (2017). Combined apatite fission-track dating, chlorine and REE content analysis by LA-ICPMS. *Science Bulletin*, *62*(22), 1497–1500. https://doi.org/10.1016/j.scib.2017.10.009

Qi, B., Hu, D., Yang, X., Zhang, Y., Tan, C., Zhang, P., & Feng, C. (2016). Apatite fission track evidence for the Cretaceous–Cenozoic cooling history of the Qilian Shan (NW China) and for stepwise northeastward growth of the northeastern Tibetan Plateau since early Eocene. *Journal of Asian Earth Sciences*, *124*, 28–41. https://doi.org/10.1016/j.jseaes.2016.04.009

Ritts, B. D., Yue, Y., & Graham, S. A. (2004). Oligocene-Miocene tectonics and sedimentation along the Altyn Tagh fault, northern Tibetan Plateau: Analysis of the Xorkol, Subei, and Aksay basins. *The Journal of Geology*, *112*(2), 207–229. https://doi.org/10.1086/381658

Ritts, B. D., Yue, Y., Graham, S. A., Sobel, E. R., Abbink, O. A., & Stockli, D. (2008). From sea level to high elevation in 15 million years: Uplift history of the northern Tibetan Plateau margin in the Altun Shan. *American Journal of Science*, *308*(5), 657–678. https://doi.org/10.2475/05.2008.01

Shao, Y., Yuan, D., Oskin, M. E., Wang, P., Liu-Zeng, J., Li, C., & Wu, Z. (2017). Historical (Yuan Dynasty) earthquake on the North Danghenanshan Thrust, Western Qilian Shan, China. *Bulletin of the Seismological Society of America*, *107*(3), 1175–1184. https://doi.org/10.1785/0120160289

Shi, W., Wang, F., Yang, L., Wu, L., & Zhang, W. (2018). Diachronous growth of the Altyn Tagh Mountains: Constraints on propagation of the northern Tibetan margin from (U–Th)/He dating. *Journal of Geophysical Research: Solid Earth*, *123*, 6000–6018. https://doi.org/10.1029/2017JB014844

Sobel, E. R., Arnaud, N., Jolivet, M., Ritts, B. D., & Brunei, M. (2001). Jurassic to Cenozoic exhumation history of the Altyn Tagh range, northwest China, constrained by ^{40}Ar/^{39}Ar and apatite fission track thermochronology. In M. S. Hendrix & G. A. Davis (Eds.), *Paleozoic and Mesozoic tectonic evolution of central Asia: From continental assembly to intracontinentaldeformation* (Vol. 194, pp. 247–267). Boulder, CO: Geological Society of America.

Sun, J., Zhu, R., & An, Z. (2005). Tectonic uplift in the northern Tibetan Plateau since 13.7 Ma ago inferred from molasse deposits along the Altyn Tagh Fault. *Earth and Planetary Science Letters*, *235*(3–4), 641–653. https://doi.org/10.1016/j.epsl.2005.04.034

Tapponnier, P., & Molnar, P. (1977). Active faulting and tectonics in China. *Journal of Geophysical Research*, *82*(20), 2905–2930. https://doi.org/10.1029/JB082i020p02905

Tapponnier, P., Xu, Z. Q., Roger, F., Meyer, B., Arnaud, N., Wittlinger, G., & Yang, J. S. (2001). Oblique stepwise rise and growth of the Tibet Plateau. *Science*, *294*(5547), 1671–1677. https://doi.org/10.1126/science.105978

Vermeesch, P., & Tian, Y. (2014). Thermal history modelling: HeFTy vs. QTQt. *Earth-Science Reviews*, *139*, 279290. https://doi.org/10.1016/j.earscirev.2014.09.010

Wang, C., Dai, J., Zhao, X., Li, Y., Graham, S. A., He, D., et al. (2014). Outward-growth of the Tibetan Plateau during the Cenozoic: a review. *Tectonophysics*, *621*, 1–43. https://doi.org/10.1016/j.tecto.2014.01.036

Wang, E. Q. (1997). Displacement and timing along the northern strand of the Altyn Tagh fault zone, northern Tibet. *Earth and Planetary Science Letters*, *150*(1–2), 55–64. https://doi.org/10.1016/S0012-821X(97)00085-X

Wang, F., Shi, W., Zhang, W., Wu, L., Yang, L., Wang, Y., & Zhu, R. (2017). Differential growth of the northern Tibetan margin: Evidence for oblique stepwise rise of the Tibetan Plateau. *Scientific Reports*, *7*(1), 41,164. https://doi.org/10.1038/srep41164

Wang, W., Zhang, P., Liu, C., Zheng, D., Yu, J., Zheng, W., et al. (2016). Pulsed growth of the West Qinling at ~30 Ma in northeastern Tibet: Evidence from Lanzhou Basin magnetostratigraphy and provenance. *Journal of Geophysical Research: Solid Earth*, *121*, 7754–7774. https://doi.org/10.1002/2016JB013279

Wang, W., Zhang, P., Pang, J., Garzione, C., Zhang, H., Liu, C., et al. (2016). The Cenozoic growth of the Qilian Shan in the northeastern Tibetan Plateau: A sedimentary archive from the Jiuxi Basin. *Journal of Geophysical Research: Solid Earth*, *121*, 2235–2257. https://doi.org/10.1002/2015JB012689

Wang, W., Zheng, W., Zhang, P., Li, Q., Kirby, E., Yuan, D., et al. (2017). Expansion of the Tibetan Plateau during the Neogene. *Nature Communications*, *8*(1), 15,887. https://doi.org/10.1038/ncomms15887

Wang, W. T., Zhang, P. Z., Kirby, E., Wang, L. H., Zhang, G. L., Zheng, D. W., & Chai, C. Z. (2011). A revised chronology for Tertiary sedimentation in the Sikouzi basin: Implications for the tectonic evolution of the northeastern corner of the Tibetan Plateau. *Tectonophysics*, *505*(1–4), 100–114. https://doi.org/10.1016/j.tecto.2011.04.006

Wang, X., Wang, B., Qiu, Z., Xie, G., Xie, J., Downs, W., et al. (2003). Danghe area (western Gansu, China) biostratigraphy and implications for depositional history and tectonics of northern Tibetan Plateau. *Earth and Planetary Science Letters*, *208*(3–4), 253–269. https://doi.org/10.1016/S0012-821X(03)00047-5

Wang, Y., Zheng, D. W., Wu, Y., Li, Y. J., & Wang, Y. Z. (2017). Measurement procedure of single-grain apatite (U-Th)/He dating and its validation by Durango apatite standard (in Chinese with English abstract). *Seismology and Geology*, *39*, 1143–1157.

Wang, Y., Zheng, J., & Zheng, Y. (2018). Mesozoic-Cenozoic exhumation history of the Qimen Tagh Range, northeastern margins of the Tibetan Plateau: Evidence from apatite fission track analysis. *Gondwana Research*, *58*, 16–26. https://doi.org/10.1016/j.gr.2018.01.014

Wolf, R. A., Farley, K. A., & Kass, D. M. (1998). Modeling of the temperature sensitivity of the apatite (U–Th)/He thermochronometer. *Chemical Geology*, *148*(1–2), 105–114. https://doi.org/10.1016/S0009-2541(98)00024-2

Wolf, R. A., Farley, K. A., & Silver, L. T. (1996). Helium diffusion and low-temperature thermochronometry of apatite. *Geochimica et Cosmochimica Acta*, *60*(21), 4231–4240. https://doi.org/10.1016/S0016-7037(96)00192-5

Wu, L., Lin, X., Cowgill, E., Xiao, A., Cheng, X., Chen, H., et al. (2019). Middle Miocene reorganization of the Altyn Tagh fault system, northern Tibetan Plateau. *Geological Society of America Bulletin*, *131*(7–8), 1157–1178. https://doi.org/10.1130/B31875.1

Wu, L., Xiao, A., Wang, L., Mao, L., Wang, L., Dong, Y., & Xu, B. (2012). EW-trending uplifts along the southern side of the central segment of the Altyn Tagh Fault, NW China: Insight into the rising mechanism of the Altyn Mountain during the Cenozoic. *Science China Earth Sciences*, *55*(6), 926–939. https://doi.org/10.1007/s11430-012-4402-7

Wu, L., Xiao, A., Yang, S., Wang, L., Mao, L., Wang, L., et al. (2012). Two-stage evolution of the Altyn Tagh Fault during the Cenozoic: New insight from provenance analysis of a geological section in NW Qaidam Basin, NW China. *Terra Nova*, *24*(5), 387–395. https://doi.org/10.1111/j.1365-3121.2012.01077.x

Yan, M., Van der Voo, R., Fang, X., Parés, J. M., & Rea, D. K. (2006). Paleomagnetic evidence for a mid-Miocene clockwise rotation of about 25° of the Guide Basin area in NE Tibet. *Earth and Planetary Science Letters*, *241*(1–2), 234–247. https://doi.org/10.1016/j.epsl.2005.10.013

Yin, A. (2010). Cenozoic tectonic evolution of Asia: A preliminary synthesis. *Tectonophysics*, *488*(1–4), 293–325. https://doi.org/10.1016/j.tecto.2009.06.002

Yin, A., Dang, Y. Q., Wang, L. C., Jiang, W. M., Zhou, S. P., Chen, X. H., et al. (2008). Cenozoic tectonic evolution of Qaidam basin and its surrounding regions (Part 1): The southern Qilian Shan-Nan Shan thrust belt and northern Qaidam basin. *Geological Society of America Bulletin*, *120*(7–8), 813–846. https://doi.org/10.1130/B26180.1

Yin, A., & Harrison, T. M. (2000). Geologic evolution of the Himalayan-Tibetan orogen. *Annual Review of Earth and Planetary Sciences*, *28*(1), 211–280. https://doi.org/10.1146/annurev.earth.28.1.211

Yin, A., Rumelhart, P. E., Butler, R., Cowgill, E., Harrison, T. M., Foster, D. A., et al. (2002). Tectonic history of the Altyn Tagh fault system in northern Tibet inferred from Cenozoic sedimentation. *Geological Society of America Bulletin*, *114*(10), 1257–1295. https://doi.org/10.1130/0016-7606(2002)114<1257:THOTAT>2.0.CO;2

Yu, J. X., Pang, J. Z., Wang, Y. Z., Zheng, D. W., Liu, C. C., Wang, W. T., et al. (2019). Mid-Miocene uplift of the northern Qilian Shan as a result of the northward growth of the northern Tibetan Plateau. *Geosphere*, *15*(2), 423–432. https://doi.org/10.1130/GES01520.1

Yuan, D. Y., Champagnac, J. D., Ge, W. P., Molnar, P., Zhang, P. Z., Zheng, W. J., et al. (2011). Late Quaternary right-lateral slip rates of faults adjacent to the lake Qinghai, northeastern margin of the Tibetan Plateau. *GSA Bulletin*, *123*(9–10), 2016–2030. https://doi.org/10.1130/B30315.1

Yuan, D. Y., Ge, W. P., Chen, Z. W., Li, C. Y., Wang, Z. C., Zhang, H. P., et al. (2013). The growth of northeastern Tibet and its relevance to large-scale continental geodynamics: A review of recent studies. *Tectonics*, *32*, 1358–1370. https://doi.org/10.1002/tect.20081

Yuan, W., Dong, J., Shicheng, W., & Carter, A. (2006). Apatite fission track evidence for Neogene uplift in the eastern Kunlun Mountains, northern Qinghai–Tibet Plateau, China. *Journal of Asian Earth Sciences*, *27*(6), 847–856. https://doi.org/10.1016/j.jseaes.2005.09.002

Yue, Y., & Liou, J. G. (1999). Two-stage evolution model for the Altyn Tagh fault, China. *Geology*, *27*(3), 227–230. https://doi.org/10.1130/0091-7613(1999)027<0227:TSEMFT>2.3.CO;2

Yue, Y., Ritts, B. D., & Graham, S. A. (2001). Initiation and long-term slip history of the Altyn Tagh fault. *International Geology Review*, *43*(12), 1087–1093. https://doi.org/10.1080/00206810109465062

Yue, Y., Ritts, B. D., Graham, S. A., Wooden, J. L., Gehrels, G. E., & Zhang, Z. (2004). Slowing extrusion tectonics: Lowered estimate of post-Early Miocene slip rate for the Altyn Tagh fault. *Earth and Planetary Science Letters*, *217*(1–2), 111–122. https://doi.org/10.1016/S0012-821X(03)00544-2

Zhang, J., Wang, Y., Zhang, B., & Zhao, H. (2015). Evolution of the NE Qinghai–Tibetan Plateau, constrained by the apatite fission track ages of the mountain ranges around the Xining Basin in NW China. *Journal of Asian Earth Sciences*, *97*, 10–23. https://doi.org/10.1016/j.jseaes.2014.10.002

Zhang, P. Z., Shen, Z., Wang, M., Gan, W., Bürgmann, R., Molnar, P., et al. (2004). Continuous deformation of the Tibetan Plateau from global positioning system data. *Geology*, *32*(9), 809–812. https://doi.org/10.1130/G20554.1

Zhang, T., Han, W., Fang, X., Miao, Y., Zhang, W., Song, C., et al. (2018). Tectonic control of a change in sedimentary environment at ~10 Ma in the northeastern Tibetan Plateau. *Geophysical Research Letters*, *45*, 6843–6852. https://doi.org/10.1029/2018GL078460

Zhang, W., Fang, X., Song, C., Appel, E., Yan, M., & Wang, Y. (2013). Late Neogene magnetostratigraphy in the western Qaidam Basin (NE Tibetan Plateau) and its constraints on active tectonic uplift and progressive evolution of growth strata. *Tectonophysics*, *599*, 107–116. https://doi.org/10.1016/j.tecto.2013.04.010

Zheng, D., Clark, M. K., Zhang, P., Zheng, W., & Farley, K. A. (2010). Erosion, fault initiation and topographic growth of the North Qilian Shan (northern Tibetan Plateau). *Geosphere*, *6*(6), 937–941. https://doi.org/10.1130/GES00523.1

Zheng, D., Wang, W., Wan, J., Yuan, D., Liu, C., Zheng, W., et al. (2017). Progressive northward growth of the northern Qilian Shan–Hexi Corridor (northeastern Tibet) during the Cenozoic. *Lithosphere*, *9*(3), 408–416. https://doi.org/10.1130/L587.1

Zheng, D., Zhang, P. Z., Wan, J., Yuan, D., Li, C., Yin, G., et al. (2006). Rapid exhumation at ~8 Ma on the Liupan Shan thrust fault from apatite fission-track thermochronology: Implications for growth of the northeastern Tibetan Plateau margin. *Earth and Planetary Science Letters*, *248*(1–2), 198–208. https://doi.org/10.1016/j.epsl.2006.05.023

Zhu, W., Wu, C., Wang, J., Zhou, T., Li, J., Zhang, C., & Li, L. (2017). Heavy mineral compositions and zircon U-Pb ages of Cenozoic sandstones in the SW Qaidam basin, northern Tibetan Plateau: Implications for provenance and tectonic setting. *Journal of Asian Earth Sciences*, *146*, 233–250. https://doi.org/10.1016/j.jseaes.2017.05.023

Zhuang, G., Hourigan, J. K., Ritts, B. D., & Kent-Corson, M. L. (2011). Cenozoic multiple-phase tectonic evolution of the northern Tibetan Plateau: Constraints from sedimentary records from Qaidam basin, Hexi Corridor, and Subei basin, northwest China. *American Journal of Science*, *311*(2), 116–152. https://doi.org/10.2475/02.2011.02

Zhuang, G., Johnstone, S. A., Hourigan, J., Ritts, B., Robinson, A., & Sobel, E. R. (2018). Understanding the geologic evolution of Northern Tibetan Plateau with multiple thermochronometers. *Gondwana Research*, *58*, 195–210. https://doi.org/10.1016/j.gr.2018.02.014

References From the Supporting Information

Galbraith, R. F. (1981). On statistical models for fission track counts. *Mathematical Geology*, *13*(6), 471–478. https://doi.org/10.1007/BF01034498

Jonckheere, R. (2003). On the densities of etchable fission tracks in a mineral and co-irradiated external detector with reference to fission-track dating of minerals. *Chemical Geology*, *200*, 41–58. https://doi.org/10.1016/S0009-2541(03)00116-5